



저작자표시-비영리-변경금지 2.0 대한민국

이용자는 아래의 조건을 따르는 경우에 한하여 자유롭게

- 이 저작물을 복제, 배포, 전송, 전시, 공연 및 방송할 수 있습니다.

다음과 같은 조건을 따라야 합니다:



저작자표시. 귀하는 원저작자를 표시하여야 합니다.



비영리. 귀하는 이 저작물을 영리 목적으로 이용할 수 없습니다.



변경금지. 귀하는 이 저작물을 개작, 변형 또는 가공할 수 없습니다.

- 귀하는, 이 저작물의 재이용이나 배포의 경우, 이 저작물에 적용된 이용허락조건을 명확하게 나타내어야 합니다.
- 저작권자로부터 별도의 허가를 받으면 이러한 조건들은 적용되지 않습니다.

저작권법에 따른 이용자의 권리는 위의 내용에 의하여 영향을 받지 않습니다.

이것은 [이용허락규약\(Legal Code\)](#)을 이해하기 쉽게 요약한 것입니다.

[Disclaimer](#)

공학박사 학위논문

**Mechanistic Understanding and Electrode
Designs for Improved Reversibility:
Case Study for Lithium Titanate Electrodes
and Lithium-Oxygen Batteries**

가역성 향상을 위한

반응 기작 이해 및 전극 설계:

리튬티타네이트 전극과 리튬산소전지

사례 연구

2019년 8월

서울대학교 대학원

화학생물공학부

배성준

Abstract

Mechanistic Understanding and Electrode Designs for Improved Reversibility: Case Study for Lithium Titanate Electrodes and Lithium-Oxygen Batteries

Seongjun Bae

School of Chemical and Biological Engineering

The Graduate School

Seoul National University

With the increasing demand for green energy, environmental-friendly power sources, like geothermal, wind and solar start to replace the fossil fuel. Electric vehicle (EV) is a representative example of this trend. The proportion of the EVs is small at this moment, however, the growth rate of the number of the EVs is very rapid. In addition, because the green energy sources suffer from a large supply fluctuation, energy storage system (ESS) is required to buffer the energy production. Enormous potential market of the EVs and the ESSs will lead to the increased consumption of the medium- and large-scale batteries. Lithium-ion batteries (LIBs) is the best system to store the energy with a large capacity due to its high energy capacity and power density. However, two problematic issues still remain to be solved for the LIBs. First, accidental explosions and fires of the EVs and ESSs are appeared occasionally. Second, despite of the high performance of LIBs, the market demands batteries with the higher energy density. To fulfill the requirement for the consumers, new type of electrodes should be developed. Here, lithium titanate ($\text{Li}_4\text{Ti}_5\text{O}_{12}$, LTO)

anode material with a high performance is proposed for the safe and high-power LIBs and lithium-oxygen battery (LOB) is studied to develop the next-generation battery system with the high energy density.

LTO anode is a replacement for the graphite anode of the LIBs. Spinel-framework structure of LTO induces a zero-strain lithium insertion/deinsertion and fast diffusion kinetics. Therefore, LTO exhibits a long lifespan and high power density. In addition, a high operating potential (1.55 V vs Li) and lacks of carbon material make the LTO battery safe. However, a low conductivity of LTO inhibits the operations at a high rate. Nanographene-surrounded LTO hybridization structure is reported here for the high rate of lithium storage. The hybridization structure was arranged by the interfacial interactions from amphipathic solvent. The amphipathic solvent acted as a bridge between the hydrophilic LTO and the hydrophobic NG. The LTO-NG hybridization was synthesized via a redox coupling between adsorbed LTO and NG. The large contact area between the LTO core and the NG sheet resulted in a high electron-conducting path. It allowed the rapid kinetics for the lithium storage and also resulted in a cyclic performance stability.

LOB is expected to overcome the energy density issue of the large-scale batteries for EVs and ESSs due to its potential high energy density. However, an irreversibility of charge/discharge reactions induces a low coulombic efficiency and lifespan. To improve the reversibility of the reactions, two type of methods were studied to control the parasitic reaction: thermodynamic approach and kinetic approach.

For the thermodynamic approach, a platinum catalyst supported on zirconia is proposed as a cathode in LOBs. Superoxide and peroxide materials occurred during battery operation, decompose the electrolyte and the carbon electrode, resulting the low reversibility of LOBs. Experimental and theoretical studies show that zirconia suppresses the reactivity of these superoxide and peroxide materials. Therefore, it is able to enhance the reversibility and lifespan in LOBs.

For the kinetic approach, the composition of the discharge product is controlled by the blockage of the reaction pathway. Stacking process of the discharge products on the electrode was investigated. And it is revealed that morphological structure of the cathode catalyst influences the composition of the discharge products. During discharge, LiO_2 -like species with a low overpotential is converted to Li_2O_2 with a high overpotential. The catalyst with large pore (> 100 nm) can inhibit the development of Li_2O_2 , because the conversion reaction is suppressed with the large pore. Therefore, catalyst with large pore results in the low overpotential and reversible reaction. This observation provides a clue to understand the behavior and kinetics of the discharge product for LOBs.

Keywords: Next-generation battery, Lithium-ion battery, Lithium titanate, Graphene, Lithium-oxygen battery, Mechanism, cathode catalyst.

Student Number: 2013-22524

Contents

Contents iv

Chapter 1. Introduction	1
1.1 Safe design of the lithium-ion batteries via advanced lithium titanate/graphene anode	1
1.2 Development of lithium-oxygen batteries for the next-generation batteries with high energy density.....	4
1.3. Objectives	8
Chapter 2. High Performance Graphene-Surrounded Lithium Titanate Anodes Using Amphipathic Solvent	10
2.1 Introduction.....	10
2.2 Experimental	12
2.2.1 Preparation of LTO-NG hybridization	12
2.2.2 Characterizations	14
2.2.3 Electrochemical characterizations.....	14
2.2.4 Computational Details	16
2.3 Results and Discussion.....	17
2.3.1 Mechanism of the graphene hybridization	17
2.3.2 Characterizations	19
2.3.3 Electrochemical measurement	23
Chapter 3. Stabilizing Discharge Products Using Electron-withdrawing Zirconia Support in Lithium-Oxygen Batteries	42

3.1 Introduction.....	42
3.2 Experimental	45
3.2.1 Fabrication of platinum deposited onto a zirconia support (Pt/ZrO₂)	45
3.2.2 Characterization.....	45
3.2.3 Electrochemical characterization	46
3.2.4 Computational details	47
3.3 Results and discussion	48
3.3.1 Charcterization.....	48
3.3.2 Electrochemical measurement	49
3.3.3 Stability measurement of the discharge products	51
3.3.4 Calculation of Li₂O₂ stability on the catalyst	53
Chapter 4. Dependence of the Physicochemical Properties of Discharge Products in Lithium-Oxygen Batteries on the reaction kinetics	65
4.1 Introduction.....	65
4.2 Experimental	68
4.2.1 Preparation of porous carbon catalyst	68
4.2.2 Characterization.....	68
4.2.3 Electrochemical characterization	68
4.3 Results and discussion	70
4.3.1 Characterization.....	70
4.3.2 Morphology and kinetics analysis of the discharge product ...	70
4.3.2 Electrochemical measurement	72
Chapter 5. Summary and Conclusions	85
Chapter 6. Recommendations for Further Research	87

Bibliography	89
국문초록	97

List of Tables

Table 2-1. Bader atomic charge analyses for the effective charge of Ti ions in bulk LTO and on the LTO (111) surface.....	26
Table 2-2. Summary of the DFT calculated adsorption energies of molecules on the LTO slab and NG at various positions.....	27

List of Figures

Figure 1-1. Development of the optimized battery system for safe and high-energy-density batteries.....	9
Figure 2-1. LTO (111) surface optimized by density functional theory calculations.....	28
Figure 2-2. (a) The minimum energy position of a water molecule near the LTO (111) surface and charge density difference map on the interface between the water and LTO. (b) Minimum energy position of a butanol molecule on the LTO surface and charge density difference map on the interface between the butanol and LTO. The red circles show hydrogen bonds on the interfaces. The isosurfaces are plotted at positive (yellow) and negative (blue) values.....	29
Figure 2-3. (a) The minimum energy position of a water molecule near the NG surface and charge density difference map on the interface between the water and NG. (b) Minimum energy position of a butanol molecule on the NG surface and charge density difference map on the interface between the butanol and NG. The isosurfaces are plotted at positive (yellow) and negative (blue) values.....	30
Figure 2-4. Schematic diagram of the procedure used in the synthesis of the LTO-NG hybridization.	31
Figure 2-5. (a) EPR signals of LTO, r-LTO and LTO-NG hybridization. (b) XPS spectra of the C1s regions of LTO-NG hybridization and o-NG.	32
Figure 2-6. (a) High-resolution TEM image of LTO-NG hybridization synthesized in an amphipathic solvent. (b) XRD pattern and (c) Raman spectroscopy for the LTO-NG hybridization material. (d) TGA analysis results of LTO-NG hybridization and LTO.	33

Figure 2-7. (a) SEM image of LTO-NG hybridization in low magnification and EDS element mapping results for (b) C, (c) Ti and (d) O species.	34
Figure 2-8. (a,b) TEM image of LTO with NG synthesized in water as the solvent.	35
Figure 2-9. (a,b) TEM image of LTO with NG synthesized in toluene as the solvent.	36
Figure 2-10. XRD patterns for LTO with NG synthesized in (a) water, (b) butanol and (c) toluene as the solvent.	37
Figure 2-11. Charge/discharge profiles of (a) LTO-NG hybridization and (b) LTO electrodes at various current densities (0.5, 1, 5 and 10 C). (c) Rate capability test of LTO-NG hybridization and LTO at various current densities during each 10 cycles. (d) Nyquist plots of LTO-NG hybridization and LTO.	38
Figure 2-12. Charge/discharge profile of LTO-NG hybridization electrode at first cycle. C-rate is 0.5 C.	39
Figure 2-13. Cyclability test of LTO/NG hybridization electrode during 100 cycles. C-rate is 0.5 C.	40
Figure 2-14. Rate capability test of LTO-NG hybridization and LTO/ μ G composite at various current densities during each 10 cycles.	41
Figure 3-1. TEM image of (a) Pt particle, (b) 10 wt% Pt/ZrO ₂	56
Figure 3-2. XRD patterns of Pt particle and Pt/ZrO ₂	57
Figure 3-3. N ₂ adsorption-desorption isotherms of Pt particle and Pt/ZrO ₂ ..	58
Figure 3-4. XPS spectra of (a) O1s, (b) Zr3d and (c) Pt4f orbital of Pt/ZrO ₂ . Olive lines of Figure 3-4c are background.....	59
Figure 3-5. Charge/discharge profiles at 0.2 mA cm ⁻² of (a) Pt/ZrO ₂ and (b) Pt particle. (c) cyclability test of Pt/ZrO ₂ and Pt particle at 0.2 mA cm ⁻²	60
Figure 3-6. (a) Galvanostatic charge/discharge test of 10, 20 wt% Pt/ZrO ₂ and	

Pt particle under TBA salt at 5 μ A, (b) Cyclability test of 10, 20 wt% Pt/ZrO ₂ and Pt particle	61
Figure 3-7. SEM image of 20 wt% Pt/ZrO ₂	62
Figure 3-8. Charge/discharge profiles without rest and with 2 days rest between charge and discharge process of (a) Pt particle, (b) 10 wt% Pt/ZrO ₂ and (c) 20 wt% Pt/ZrO ₂	63
Figure 3-9. (a) Calculated binding energy of (Li ₂ O ₂) _n (n = 1,2,3) adsorbed on Pt (111) and ZrO ₂ (-111). (b) Charge density difference of Li ₂ O ₂ adsorbed on Pt (111) and ZrO ₂ (-111). (c) Calculated binding energy of (Li ₂ O ₂) _n (n = 1,2,3) adsorbed on Pt (200) and ZrO ₂ (111). (d) Charge density difference of Li ₂ O ₂ adsorbed on Pt (200) and ZrO ₂ (111). The isosurfaces are plotted at positive (yellow) and negative (blue) values	64
Figure 4-1. SEM images of (a) SPC and (b) LPC. (c) Pore size distributions and (d) N ₂ adsorption/desorption isotherms of SPC and LPC	75
Figure 4-2. XRD patterns of SPC and LPC	76
Figure 4-3. SEM images of discharged SPC electrodes at the indicated capacities (a) 100 mAh g ⁻¹ and (b,c) 1000 mAh g ⁻¹ and (d) charged to 4 V electrode.	77
Figure 4-4. SEM images of discharged LPC electrodes at the indicated capacities (a) 100 mAh g ⁻¹ and (b,c) 1000 mAh g ⁻¹ and (d) charged to 4 V electrode.	78
Figure 4-5. Raman spectra of discharged and charged to 4V SPC electrodes	79
Figure 4-6. Rate capability test of (a) SPC and (b) LPC. (c) The degradation of LiO ₂ with respect to time	80
Figure 4-7. Charge/discharge profiles of (a) SPC and (b) LPC with a limited capacity of 1000 mAh g ⁻¹ . The current density is 400 mA g ⁻¹	81
Figure 4-8. XRD patterns of SPC and LPC electrodes after 40 cycles	82

Figure 4-9. SEM images of (a) SPC and (b) LPC after 40 cycles.83

Figure 4-10. Nyquist plots of (a) SPC and (b) LPC electrodes before and after
40 cycles. (c) Equivalent circuits for pristine electrode and
cycled electrode.84

Chapter 1. Introduction

1.1 Safe design of the lithium-ion batteries via advanced lithium titanate/graphene anode

Lithium metal is the lightest metal (6.94 g/mol, 0.534 g/cm³) and it has very low standard reduction potential (-3.04 V vs standard hydrogen electrode). Therefore, a battery based on lithium and lithium ion has a high energy density [1,2]. However, there is severe problematic issue to the batteries with lithium anode. During charge/discharge cycles, dendrite lithium metal appears on the anode/electrolyte interface due to the repeated stripping/plating. This phenomenon causes fire and explosion by short-circuit and thermal runaway in the lithium metal batteries [3,4].

To avoid the dendritic growth of lithium metal, host materials, which can insert the lithium ion were developed as the anode for the lithium batteries [5,6]. This technology is known as lithium-ion batteries (LIBs). LIBs relieve the dendritic formation of lithium metal because lithium exists as the ionic state rather than metallic state. Therefore, LIBs is much safer than the lithium metal batteries. Various host materials for the anode, like lithium alloy [7,8] and metal oxide [6, 9] had been developed since 1970s. After the first commercialization of LIBs in 1991, carbon, especially graphite is almost the only material for the

anode [2]. The potential of the graphite is similar with lithium metal (0.15 V vs Li) and graphite exhibits a high energy density (373 mAh g⁻¹) and high chemical stability.

However, the dendrite of lithium metal still appears on the graphite anode with the repeated charge/discharge [10,11]. As a result, explosion and fire hazard are not avoidable to the LIBs. As the application of LIBs changes from the power source for mobile devices to the energy storage for electric vehicles or energy storage systems, the scale and risk of the accident becomes severe [12-14]. Considering this trend, manufacturers and consumers start to deal with the safety issue seriously.

To guarantee the safety of the LIBs, high voltage anode materials can be an attractive candidate. High voltage anode materials operate over 0.8 V vs Li. Therefore, it is free of the the dendrite lithium growth. Lithium titanate, Li₄Ti₅O₁₂ (LTO) is intensively studied high voltage anode material. Spinel structure of LTO offers a zero-strain lithium ion insertion/deinsertion and causes an excellent cyclic stability, flat potential plateau and high power density [15-17]. Due to the high voltage of LTO (1.55 V vs Li), the safety of LIBs with LTO anode is extremely high. Although a low theoretical capacity (175 mAh g⁻¹) and low conductivity (~10⁻¹³ S cm⁻¹) are critical drawbacks of LTO, the outstanding safety and good power density of LTO is the important

characteristics for the large-scale LIBs [18,19].

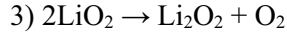
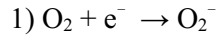
The specific capacity of LTO is unchangeable, however, the conductivity can be improved by a hybridization with the carbon. Carbon coating is a prevalent method to enhance the rate performance of the electrode materials due to its easiness of techniques and low cost [20,21]. Generally, carbon sources are mixed with LTO or LTO precursor, and followed heat-treatment makes LTO/carbon complex. Although the methodology is simple and suitable for the large-scale production, uniform formation of the LTO/carbon complex is still a problem. Graphene, which has a low-dimensional morphology is an appropriate carbon material to develop uniform complex with a high conductivity [22,23]. Various forms of LTO in 3D-structured graphene have been proposed by the researchers [24-26]. However, because graphene is too large compared to LTO, the morphology of LTO/graphene is usually LTO anchored on graphene structure. Due to the small contact area between LTO and graphene, the conductivity of LTO/graphene cannot exhibit the expected values. To get over this limitation, the development of the ideal graphene hybridization methodology is highly desirable.

1.2 Development of lithium-oxygen batteries for the next-generation batteries with high energy density

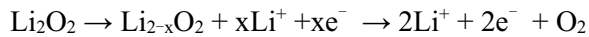
Battery is a bottleneck of the specification of the EVs. The limitation of the driving range of the EVs is determined by the performance of the batteries [27,28]. The driving range of Tesla model 3, which is the latest model of the EV is about 500 km. The weight of this battery is about 470 kg. It is 12 times larger than the weight of the equivalent gasoline assuming that the mileage of the gasoline is 10km L⁻¹. Current EVs have enough specification for the ordinary driving. However, to develop the best design of the EVs, the increase of the battery energy density will be an important issue in future. Therefore, researchers start to focus on the next-generation battery systems rather than LIBs, because conventional LIB meets the theoretical limit of the specific energy density [29].

Lithium-oxygen batteries (LOBs) has the highest energy density among the next-generation battery system (3.5 kWh kg⁻¹) [30,31]. LOBs are composed with lithium metal anode, electrolyte, porous cathode catalyst and the oxygen gas from the outside. The reaction mechanism of LOBs are as followed [32,33]

Discharge



Charge



During the discharge, lithium metal is stripped on the anode. Lithium ion reacts with reduced oxygen ion (O_2^-) and forms lithium superoxide (LiO_2) on the cathode. LiO_2 is converted to lithium peroxide (Li_2O_2) by a disproportionation reaction. Because Li_2O_2 is not soluble to the electrolyte, solid Li_2O_2 is precipitated on the cathode surface. On charge process, lithium metal is plating on the anode and Li_2O_2 is decomposed to the oxygen gas and lithium ion on the cathode.

There are two critical problems on the LOBs First, intermediates and final product (O_2^- , LiO_2 , Li_2O_2) are not stable [34,35]. These materials react with the electrolyte and the carbon electrode easily. As a result, nonconductive Li_2CO_3 passivates the porous cathode and the byproducts like water react with lithium metal causing nonconductive LiOH layer on the anode [36,37]. Therefore, LOBs have a low reversibility, resulting a low coulombic efficiency and

lifespan. Second, high overpotential is required to decompose the final product, Li_2O_2 . A conventional carbon electrode needs over 4 V vs Li to decompose Li_2O_2 . In this circumstance, the electrolyte is also electrochemically reduced and produces the byproducts, such as Li_2CO_3 and water [38,39]. These materials hinder the operation of LOBs by the same way with the first problem above.

To improve the performance of LOBs, various catalysts for OER/ORR including noble metal [40, 41], metal oxide [42,43], nitride [44,45] and sulfide [46,47] have been proposed to the porous cathode catalyst. The main purpose of these researches are decrease of the overpotential, which causing the parasitic reactions. Noticeable results have been obtained by many studies, however, screening of the materials is not enough to develop the cathode catalyst. For the rational design of the cathode catalyst, the research based on the mechanism of LOBs is necessary. Recently, researchers start to develop the cathode catalyst with the consideration of the mechanism. For example, thermodynamic stabilization of the unstable discharge product [48,49] and reactive intermediate stabilizer [50] are proposed to enhance the reversibility of LOBs. Still, there are many unclear nature of LOBs, which affects the

performance. Therefore, upcoming studies about LOBs should focus on the understanding of the mechanism for LOBs to design the rational cathode catalyst.

1.3. Objectives

The objectives of this thesis are the development of the electrode material for the safe LIBs (Chapter 2) and the design of the electrodes for advanced next-generation batteries, LOBs (Chapter 3, 4) (Figure 1-1).

In following section, Chapter 2, graphene surrounded LTO with a high rate capability is developed. To achieve this, uniform graphene deposition technique were derived by the bridging of the amphipathic solvent with redox coupling between LTO and graphene.

In Chapter 3, the stabilization of the intermediates and discharge products is proposed. A platinum catalyst with high performance is deposited on zirconia support to enhance both the catalytic activity and the reversibility of the charge/discharge reactions.

Finally, control of the composition of the discharge product by tuning the reaction rate of the intermediates was discussed. Kinetic study revealed that the blockage of the contact between the discharge product and the electrolyte induces the discharge product with a low overpotential.

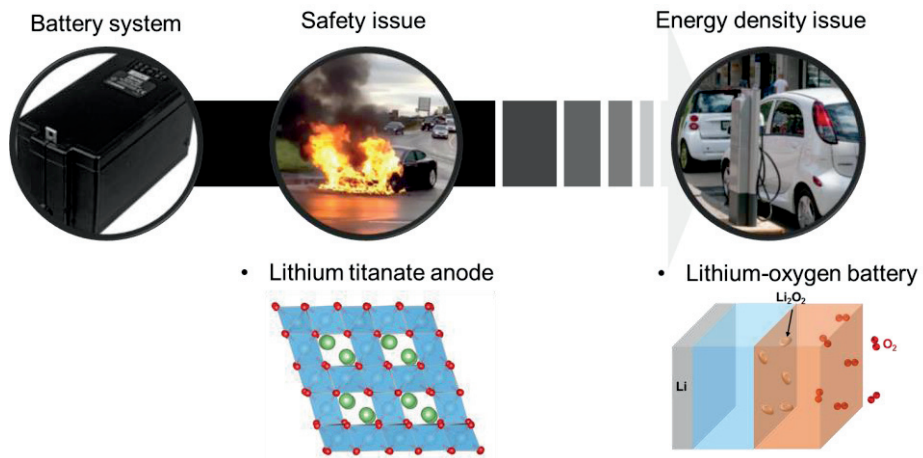


Figure 1-1. Development of the optimized battery system for safe and high-energy-density batteries.

Chapter 2. High Performance Graphene-Surrounded Lithium Titanate Anodes Using Amphipathic Solvent

(Reproduced with permission from [S. Bae[†] and I. Nam[†] et al., ACS Appl. Mater. Interfaces, 2015, 7, 30, 16565-16572] Copyright [2019] American Chemical Society)

2.1 Introduction

Spinel LTO is a candidate for the potential alternative material to replace the current graphite anode. During charging, intercalation of the lithium atoms into spinel LTO leads to a phase change of LTO from a spinel to a rock-salt structure [51,52]. Parameter change is not occurred during the insertion/deinsertion reactions of LTO, which is the reason that LTO is the zero-strain insertion material. Due to its structural advantages, LTO has excellent lithium ion insertion/deinsertion reversibility, structural stability, fast lithium ion diffusivity, and good cyclability [15-17]. In addition, the high operating voltage of LTO (1.55 V vs Li) prevents the formation of solid/electrolyte interface (SEI) and dendritic lithium metal. Despite these advantages, insulative characteristics

of LTO induces severe polarization at the electrode and low rate capability [53,54]. Before solving the conductivity issue, LTO is not suitable for the anode material in next-generation, high-power LIBs.

To enhance the electronic conductivity of LTO, several methodologies, including nanostructuring [55,56] and doping by various atoms [57,58], have been studied. Among them, a composite of LTO with allotropes of carbon would effectively confer a high conductivity to LTO and has merits in terms of process convenience. In particular, carbon coating of LTO particles are capable of achieving a high-power with a high tap density (over 1.7 g cm^{-3}) [59]. Among the allotropes of carbon, graphene has the most desirable characteristics for use as a substrate for hosting active materials in LIBs due to the excellent conductivity, chemical stability, a regular framework, and a high surface area [60,61]. The sheet and particle (wrapping cloth) structure of conventional graphene composites, however, results in a low contact area between the active material/graphene and a relatively low tap density because a graphene sheet, having an order of magnitude larger size compared to active particles, is not an ideal carbon-coating structure [62-64]. To the best of our knowledge, this study is the first attempt to provide theoretical and experimental proof of LTO-

nanographene (NG) hybridization materials for use as a high-power LIB anode material. Because the size of the LTO particle is larger than that of the NG sheet, an adsorption phenomenon between LTO and NG allows the NG sheets to uniformly surround the LTO particle, and consequently, an NG-surrounded LTO structure is produced. Here, we report on the optimization of the adsorption properties between LTO and an NG interface. The property optimization involved the use of density functional theory (DFT) calculations that enabled an LTO-NG hybridization structure to be prepared. Tethering NG on the surface of LTO allows an intimate level of contact between the conductive surface and the inner active material. The graphene-decorated composites exhibited a high specific capacity and good rate capability.

2.2 Experimental

2.2.1 Preparation of LTO-NG hybridization

To surround the surface of LTO with NG, LTO particles were first reduced. In this step, the Ti^{4+} ion of LTO surface was reduced to the unstable Ti^{3+} state, which induces a redox reaction between reduced LTO (r-LTO) and oxidized

NG (o-NG). A 0.2 g sample of r-LTO was dispersed in 60 mL of water, 1-butanol, or toluene. A 5 wt % o-NG suspension (0.1 g ml^{-1}) was added to the suspension under vigorous stirring. The resulting suspension was stirred for 1 h, transferred to a Teflon-sealed autoclave, and maintained at $180 \text{ }^{\circ}\text{C}$ for 24 h. The resulting composite was centrifuged and washed with acetone. The r-LTO was fabricated by hydrogenation. The reaction was carried out in a flow-type quartz reactor in an electric furnace. A 1 g sample of commercial LTO ($\sim 500 \text{ nm}$) was heated at $600 \text{ }^{\circ}\text{C}$ for 3 h under an atmosphere of N_2 with H_2 . The ratio of H_2/N_2 is 1/10. The heating rate was controlled at $5 \text{ }^{\circ}\text{C min}^{-1}$. o-NG was synthesized by the two-step oxidation of graphite. Graphite was first oxidized by an improved Hummer's method [65]. A 0.1 g sample of as-synthesized graphite oxide was added to 100 mL of a concentrated H_2SO_4 solution and 0.3 g of KMnO_4 was slowly added over a 3 h period at $45 \text{ }^{\circ}\text{C}$, with vigorous stirring. The mixture was cooled in an ice bath, and 100 mL of a H_2O_2 solution (90 mL of water + 10 mL of 30 wt % H_2O_2) was then slowly added. The solution was then stirred for over 1 h. The resulting solution was sonicated for 30 min and washed with water and HCl. The washed precipitate was suspended and exfoliated in 10 mL of water.

2.2.2 Characterizations

The surface morphology of LTO-NG hybridization was characterized by high-resolution transmission electron microscopy (HR-TEM, JEOL, JEM-3010). Field-emission scanning electronic microscopy (FE-SEM, Carl Zeiss, AURIGA) and energy-dispersive X-ray spectroscopy (EDS) were used to prove the uniformity of the graphene surrounding. An X-ray diffractometer (XRD, Rigaku, D/max-2500/PC) was utilized to confirm the crystalline and elemental structure of the composite. The mass ratio of NG was calculated on the basis of data obtained from a thermogravimetric analyzer (TGA, Versa Therm, Thermo Scientific) with a heating rate of $10\text{ }^{\circ}\text{C min}^{-1}$ in air. Electron spin resonance (ESR, JEOL, JES-TE200) spectroscopy and X-ray photoelectron spectroscopy for C 1s (XPS, CE Elantech, Flash2000) were carried out to investigate the valency of the ion and bonding.

2.2.3 Electrochemical characterizations

Electrochemical measurements were carried out using CR2032-type coin cells at room temperature. The working electrode was prepared by mixing 80

wt % of the NG-LTO hybridization or pure LTO as the active material, 10 wt % Super P as a conductive additive, and 10 wt % poly(vinylidene difluoride) (PVDF) as a binder of the total electrode mass. These three components were mixed using N-methyl-2-pyrrolidone (NMP) as a solvent to produce a slurry. The slurry was uniformly loaded on a Cu foil using doctor-blade technique and was compressed to prepare a film-type electrode. The electrode loading of the active materials was 1 mg cm^{-2} . After drying for 12 h under vacuum at $120 \text{ }^\circ\text{C}$, the cells were assembled in an Ar-filled glovebox with lithium foil as an anode and a 1.15 M LiPF_6 solution of dissolved in 13:5:2 (v/v/v) ethylene carbonate/ethyl-methyl carbonate/diethyl carbonate was adopted as electrolyte. A galvanostatic charge/discharge analysis was carried out with an automatic battery cycler (WBCS3000, Wonatech) in the potential range of 0.8–3.0 V vs Li. Electrochemical impedance spectroscopy measurements were performed at $E = 1.55 \text{ V}$. The frequency range was 0.001–100 kHz under ac stimulus with 10 mV amplitude using a ZIVE SP2 potentiostat (Wonatech).

2.2.4 Computational Details

First-principles calculations were carried out on the basis of periodic DFT using a generalized gradient approximation (GGA) within the Perdew–Burke–Ernzerhof (PBE) exchange-correction functional [66,67]. We used the projector-augmented wave (PAW) method for describing ionic cores as implemented in the Vienna ab initio simulation package (VASP) [68]. To incorporate van der Waals interactions, the DFT-D2 empirical correction of Grimme was included [69]. DFT+U within Dudarev’s approach was also used with $U_{\text{eff}} = 3.5$ to account for on-site coulomb interactions in the localized d orbital of Ti [70]. The wave functions were constructed from the expansion of plane waves with an energy cutoff of 400 eV. A $1 \times 1 \times 1$ k-point mesh described in Monkhorst–Pack method was used to sample the Brillouin zone. The electronic optimization steps were converged self-consistently over 10^{-4} eV per formula unit.

2.3 Results and Discussion

2.3.1 Mechanism of the graphene hybridization

To fabricate a graphene surrounded structure, controlling the homogeneity of the reaction and the uniformity of the precursor concentrations are very important. To satisfy these prerequisites, the NG was synthesized by a double-oxidizing method from graphite. A subsequent synthesis approach is similar to the heat-up method used in the fabrication of highly uniform nanocrystals intended for commercial use [71,72]. Based on this method, we substituted the reactive precursor for LTO particles with a size of ~ 200 nm and NG sheets with ~ 30 nm size. As a consequence, the choice of solvent is critical because the solvent determines the uniformity of the reactants (LTO and NG) and the interfacial chemistry between LTO and NG. The solvent candidates considered for the reaction were water, toluene, and butanol, which represent a polar, nonpolar, and amphipathic solvent, respectively.

The mechanism responsible for the adsorption of the reactants at the atomic surface level is investigated using DFT calculations. The (111) plane of LTO has a minimum surface energy of 0.63 J m^{-2} , and it can be regarded as a

representative LTO surface (Figure 2-1) [73-75]. The results of Bader charge analyses are presented in Table 2-1. The exposed atoms on the (111) plane are Ti that have effective average charge of +1.19 e. The average values for bulk Ti in the same location are +1.98 e, which means that the average excessive charge on the surface atoms is $\Delta(-0.79 \text{ e})$. In the charge density distribution, the surface charge is larger than that of the bulk structure because of the various dangling bond states.

LTO is a polarizable material, and the absorption of a solvent on LTO is attributed to hydrogen bonding. Polar (water) and the amphipathic solvent (butanol) both have hydroxyl functional groups that are bonded to the LTO surface with the adsorption energies of -0.53 and -1.16 eV , respectively. In the plots for the charge density difference, both of them show a hybridized region between Ti on the surface of LTO and O in the solvent, indicating the occurrence of hydrogen bonding (red dashed circles, Figure 2-2). In contrast, NG has nonpolar properties and is surrounded by solvent molecules by van der Waals interactions. In water, the adsorption energy of the solvent molecule onto NG is positive (5.71 eV), indicating that NG and polar molecules repulse one another (Figure 2-3a). The amphipathic solvent, however, has a carbon

backbone and a relatively larger area, which permits NG to readily bond to the backbone of the molecule. The charge density difference plot of the NG/butanol interface is shown in Figure 2-3b. In this case, electronic hybridization was found in NG and the backbone of the molecule interface. The charge accumulations and reductions are vertically superposed between NG and the molecule, suggesting the existence of van der Waals interactions between the C atoms. The calculated total energies are summarized in Table 2-2. Because the absorption direction of the amphipathic molecule on LTO and NG is opposite, the overall effect is a uniform adsorption of LTO and NG with repulsions between LTO/LTO and NG/NG interfaces. The optimized absorbed states of LTO and NG in the various solvents are summarized in Figure 3. Consequently, the amphipathic solvent is adsorbed on LTO and NG, and the composite is well-dispersed in an amphipathic solvent that functions as a glue between the two reactants.

2.3.2 Characterizations

Figure 2-4 illustrates the experimental process used to prepare LTO-NG hybridization. The graphite oxide contained small amounts of O-containing functional groups on the basal plane. To fabricate NG, the graphite oxide was

exfoliated to graphene oxide and then reoxidized for cracking [76, 77]. The reoxidizing method first generates a partially oxidized NG (o-NG). The thickness and size of o-NG varied in the ranges of 0.8–2.0 nm and 30–40 nm, respectively [77]. In the next step, the surface of LTO was partially reduced by H₂ gas at 600 °C (r-LTO). Because the Ti⁴⁺ state on the surface of LTO is unstable after the H₂ treatment, reoxidization with oxidants such as o-NG proceeds readily [58]. As verified through the DFT calculations reported above, the formation of an NG-surrounded LTO results in the minimization of energy in an amphipathic solvent. In the same way, r-LTO/o-NG in amphipathic solvent easily forms a surrounded structure. The subsequent heating of the solution permits a coupled redox reaction between r-LTO and o-NG. During the reoxidizing of the LTO surface, o-NG is simultaneously reduced, and NG is bonded to the surface of LTO. EPR spectroscopy was used to verify the reoxidizing reaction of LTO (Figure 2-5a). O vacancies in r-LTO were observed, which is caused by the paramagnetic characteristics of Ti³⁺ ions of the surface related to a g value of 1.96 [78]. In contrast, no EPR signals were detected for pure LTO or LTO-NG hybridization, which means that r-LTO is oxidized via the formation of a graphene-surrounded structure. The reduction

of o-NG was proven by XPS analyses for the C 1s region, before and after the LTO reoxidizing process (Figure 2-5b). Before the reaction, a peak corresponding to C–O bonds was observed for o-NG. After the reaction, however, the peak was largely decreased. The mechanism responsible for the coupled redox reaction was verified in recent research regarding the synthesis of Mn₃O₄/graphene hybrids [79]. The synthesis procedure for producing LTO-NG hybridization does not involve an additional reduction of graphene after the heat treatment, which is another distinct advantage of this method because a graphene reduction step can consume a considerable amount of energy and produce toxic byproducts [65].

The morphology of LTO-NG hybridization was investigated by HR-TEM (Figure 2-6). LTO core and NG sheet are clearly observable, which is quite different from conventional graphene/particle composites that are based on the use of a micrometer-sized graphene sheet [62-64, 79]. The lattice with a 0.48 nm is well-matched with (111) surface of LTO and lattice with a 0.34 nm is d-spacing of the graphite. In the Raman spectroscopy, D band and G band of graphene is observed due to NG sheet. In the XRD patterns of LTO-NG hybridization, the major spectral peaks are consistent with the peaks for the

spinel structure of LTO (JCPDS, Card no. 26-1198, Figure 2-6c). No diffraction peaks corresponding to a stacked graphene were observed in the structure because its content in NG sheet is very small, and the peak for an NG sheet with a thickness of a few nanometers is very broad, according to the Scherrer equation. The NG-surrounded LTO structures were also proved by SEM-EDS elemental mapping analyses at a low magnification. As shown in Figure 2-7, C atoms are present on all surfaces of the materials, analogous to O and Ti species, which means that the materials uniformly included C atoms. In conclusion, this result proves that NG sheets are uniformly deposited on LTO particles and that the structures were synthesized with a high degree of reproducibility. On the basis of the weight loss of the material around 700 °C (TGA, Figure 2-6d), we concluded that NG sheet functioning as an electron path represents only 1.3 wt% of LTO-NG hybridization. Therefore, the gravimetric performance fading and ionic resistance because of an NG sheet are negligible. For the control analyses, we also conducted heat treatments of r-LTO and o-NG in water and toluene. As shown in the optical images in Figure 2-8, r-LTO and o-NG also acted similar to LTO and NG, respectively, in these solvents. Because LTO and NG are repulsive with respect to each other in water, LTO/NG synthesized in water

revealed that LTO and NG are located separately. In toluene, the material forms large aggregates that prevent ionic motion from the electrolyte to the inner material causing a substantial decrease in electrochemical performance. The presence of an aggregate state was verified by TEM images of LTO/NG based on toluene (Figure 2-9).

In these solvents. Because LTO and NG are repulsive with respect to each other in water, LTO/NG synthesized in water revealed that LTO and NG are located separately (Figure 2-8). The XRD pattern of the water-based LTO/NG had a (002) peak for graphite, which is indicative of a graphene ABAB stack (Figure 2-10). The result shows that the laminating graphene structure is separate from the other components.

2.3.3 Electrochemical measurement

We evaluated the electrochemical performance of LTO-NG hybridization as an anode for LIBs (Figure 2-11). The values for specific capacity were calculated on the basis of the total mass of the active materials. The capacity from NG sheet was negligible considering the low weight ratio. As demonstrated in the charge and discharge profiles, the electrochemical performances of LTO are markedly improved through its surrounding by NG. The lithium storage

capability of LTO increased from 130 mAh g⁻¹ at a current rate of 0.5 C for pure LTO electrodes to 147 mAh g⁻¹ even at a tenfold higher current rate of 5 C for LTO-NG hybridization electrodes. At 0.5 C, LTO-NG hybridization showed 165 mAh g⁻¹ (94% of the theoretical values), and over 135 mAh g⁻¹ of the capacity could be still retained for LTO-NG electrodes at high current rates of 10 C. Figure 2-11c shows a comparison of the rate capability of LTO-NG hybridization and that of pure LTO at various rates during 10 cycles. Capacity fading is generally negligible in the case of LTO, which is one of the strengths of the material considering its zero-strain structure. LTO-NG hybridization maintained not only a high rate capability, but also capacity fading was negligible because the surrounded structure contains tightly bonded interfaces as the result of the redox coupling effect and large interfacial area of the material. Aided by the conductive NG network throughout the entire material, numerous electron transport pathways are produced. As a consequence, electron transport is more effective, and the electrical conductivity of the electrode is improved.

To compare LTO-NG hybridization and pure LTO, we also conducted electrochemical impedance spectroscopy analyses (Figure 2-11d). In the

Nyquist plot, the semicircle represents the charge transfer resistance of the synthesized materials (R_{ct}). R_{ct} of LTO-NG hybridization is 186Ω , which is 359Ω for the value of pure LTO. The results indicate that NG reduces the resistance of the material in LTO-NG hybridization.

The Coulombic efficiency of LTO-NG hybridization was over 95% for the first cycle, indicating that irreversible capacity loss is also negligible (Figure 2-12). In addition, the material maintained a capacity of over 97% of the original value at the initial cycle even after 100 charge-discharges (Figure 2-13). These results indicate that LTO-NG hybridization can be used practically in high-rate energy-storage devices, such as electric vehicles. For a control experiment, we fabricated a LTO/microsized graphene (LTO/ μ G) composite. As shown in Figure 2-14, LTO/ μ G electrode shows a lower capacity and lower rate capability than those of LTO-NG hybridization electrode. The result also proves that LTO-NG hybridization is the one of optimized structures of LTO with carbon allotropes to increase the electrical performances of electrodes.

Table 2-1. Bader atomic charge analyses for the effective charge of Ti ions in bulk LTO and on the LTO (111) surface.

Ion	Bulk	Surface	Surface residual charge / $\Delta(-e)$
	Charge / -e	Charge / -e	
Ti	1.99	1.18	-0.81
	1.99	1.19	-0.80
	1.97	1.18	-0.79
	1.98	1.12	-0.86
	1.99	1.13	-0.86
	1.97	1.15	-0.82
	1.98	1.29	-0.69
	1.96	1.28	-0.68

Table 2-2. Summary of the DFT calculated adsorption energies of molecules on the LTO slab and NG at various positions.

Molecule	Surface slab	
	LTO	NG
Water	-0.53	5.71 (not binding)
Adsorption energy / eV		
Batanol	-1.16	-0.25

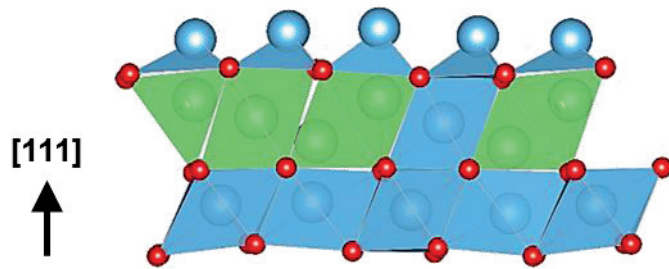


Figure 2-1. LTO (111) surface optimized by density functional theory calculations.

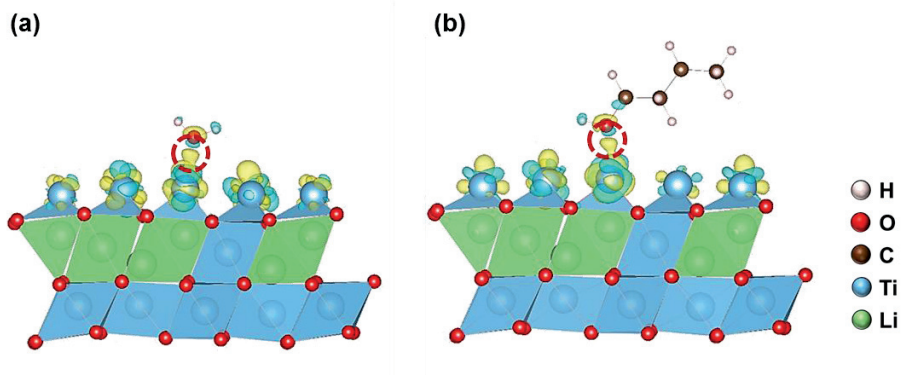


Figure 2-2. (a) The minimum energy position of a water molecule near the LTO (111) surface and charge density difference map on the interface between the water and LTO. (b) Minimum energy position of a butanol molecule on the LTO surface and charge density difference map on the interface between the butanol and LTO. The red circles show hydrogen bonds on the interfaces. The isosurfaces are plotted at positive (yellow) and negative (blue) values.

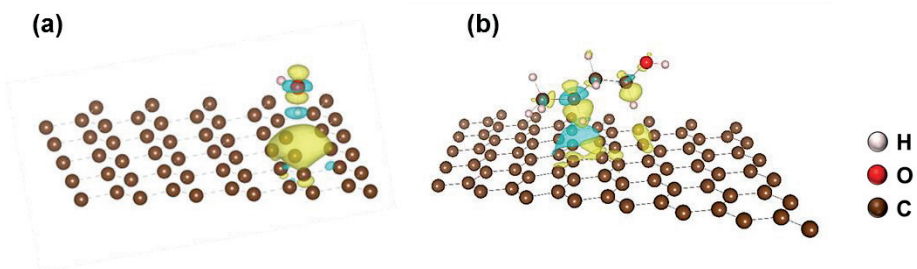


Figure 2-3. (a) The minimum energy position of a water molecule near the NG surface and charge density difference map on the interface between the water and NG. (b) Minimum energy position of a butanol molecule on the NG surface and charge density difference map on the interface between the butanol and NG. The isosurfaces are plotted at positive (yellow) and negative (blue) values.

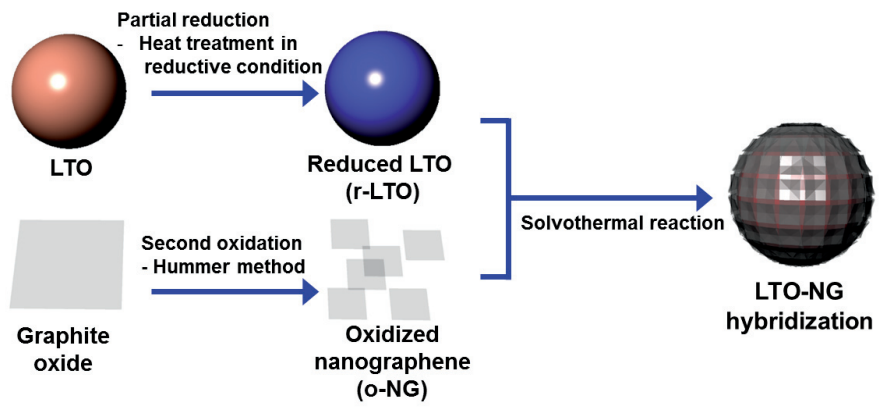


Figure 2-4. Schematic diagram of the procedure used in the synthesis of the LTO-NG hybridization.

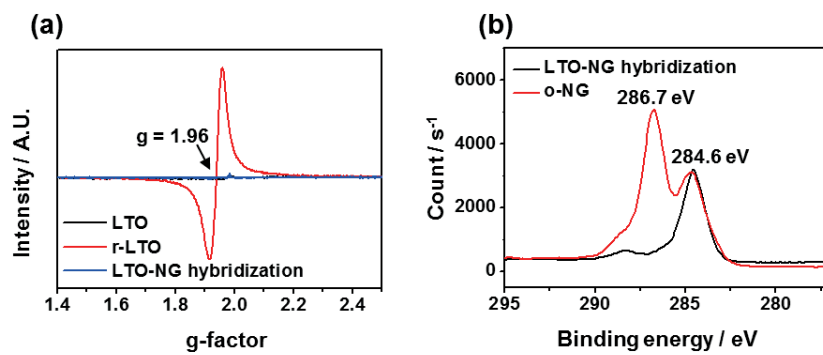


Figure 2-5. (a) EPR signals of LTO, r-LTO and LTO-NG hybridization. (b)

XPS spectra of the C1s regions of LTO-NG hybridization and o-NG.

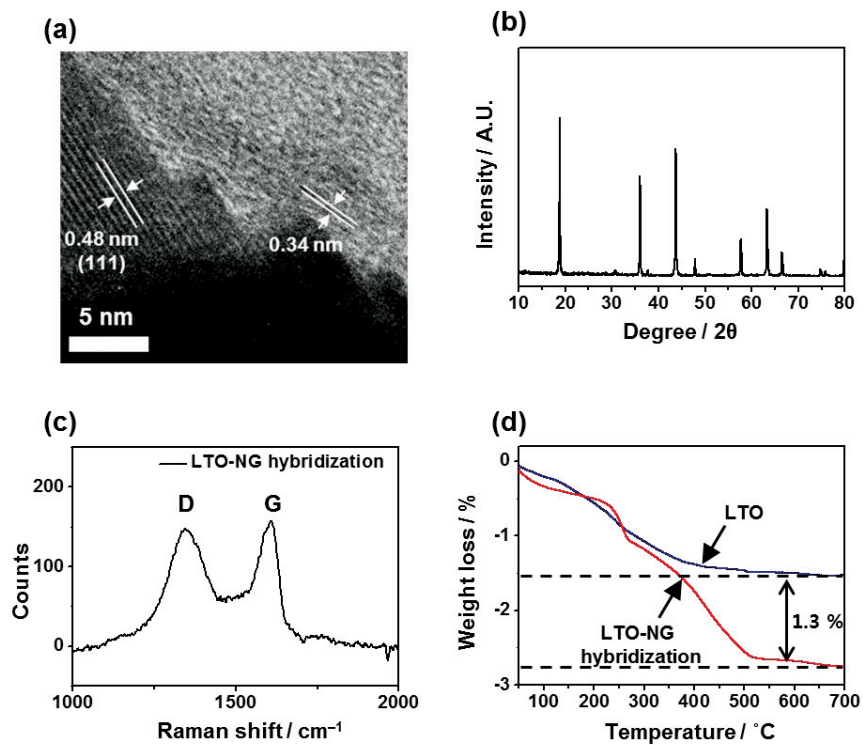


Figure 2-6. (a) High-resolution TEM image of LTO-NG hybridization synthesized in an amphipathic solvent. (b) XRD pattern and (c) Raman spectroscopy for the LTO-NG hybridization material. (d) TGA analysis results of LTO-NG hybridization and LTO.

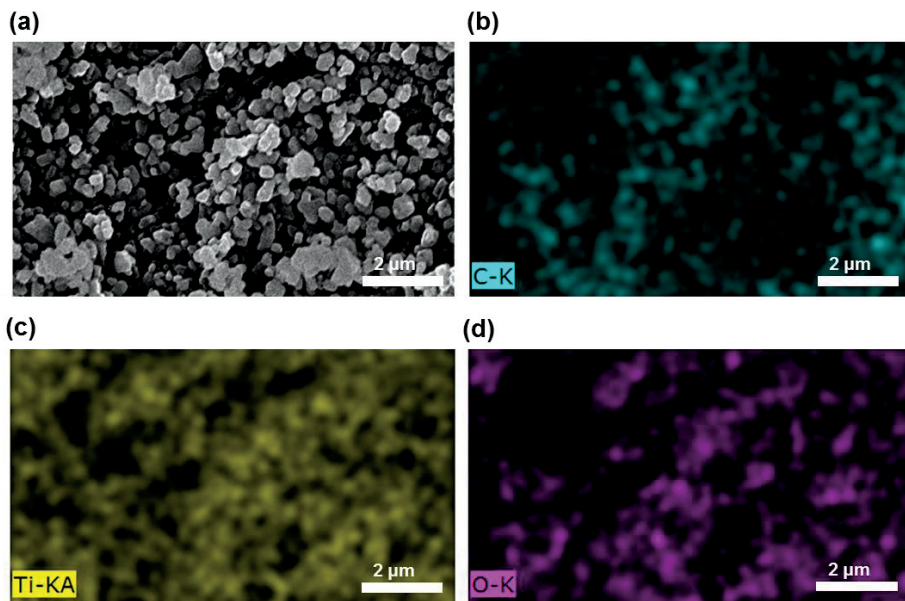


Figure 2-7. (a) SEM image of LTO-NG hybridization in low magnification and EDS element mapping results for (b) C, (c) Ti and (d) O species.

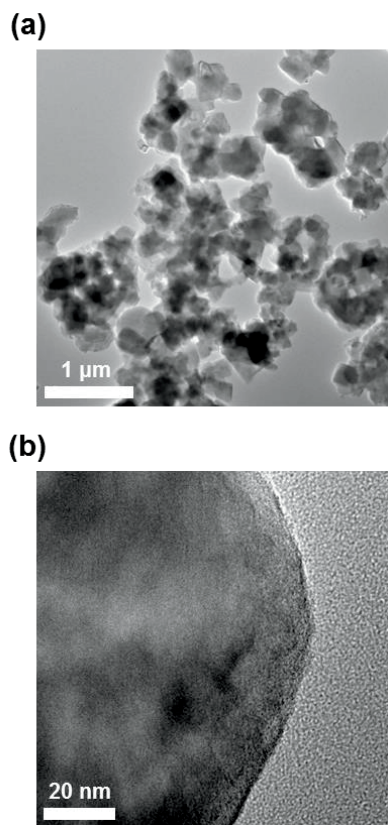


Figure 2-8. (a,b) TEM image of LTO with NG synthesized in water as the solvent.

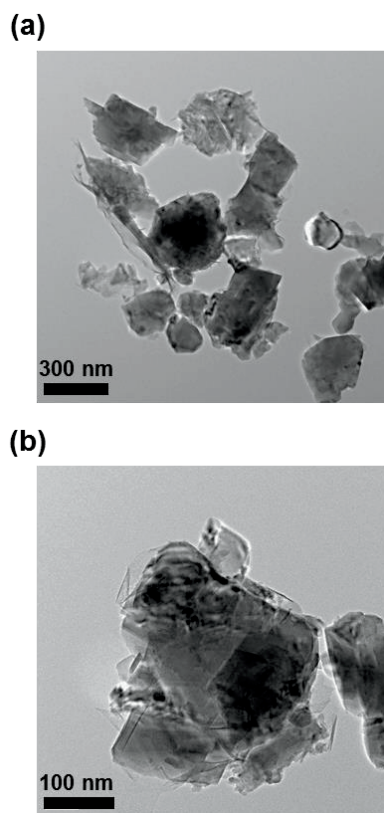


Figure 2-9. (a,b) TEM image of LTO with NG synthesized in toluene as the solvent.

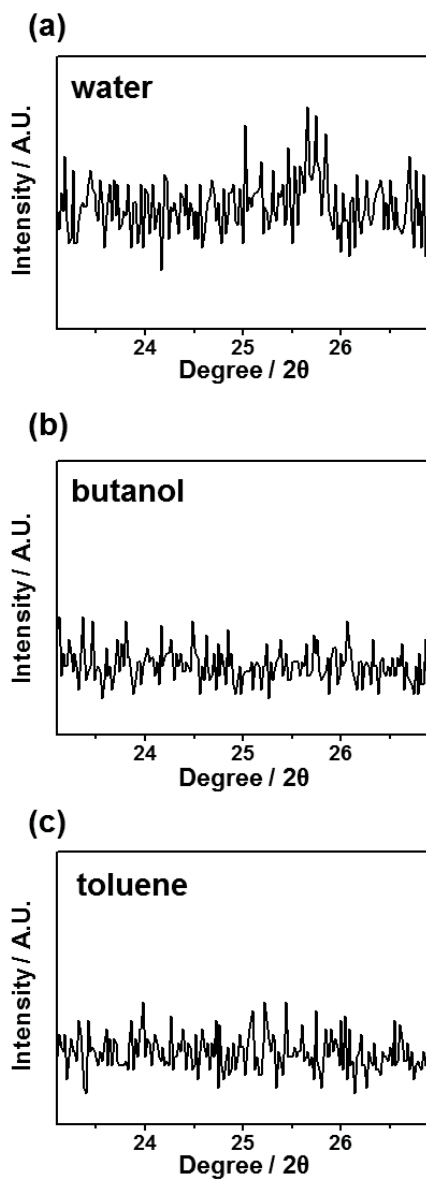


Figure 2-10. XRD patterns for LTO with NG synthesized in (a) water, (b) butanol and (c) toluene as the solvent.

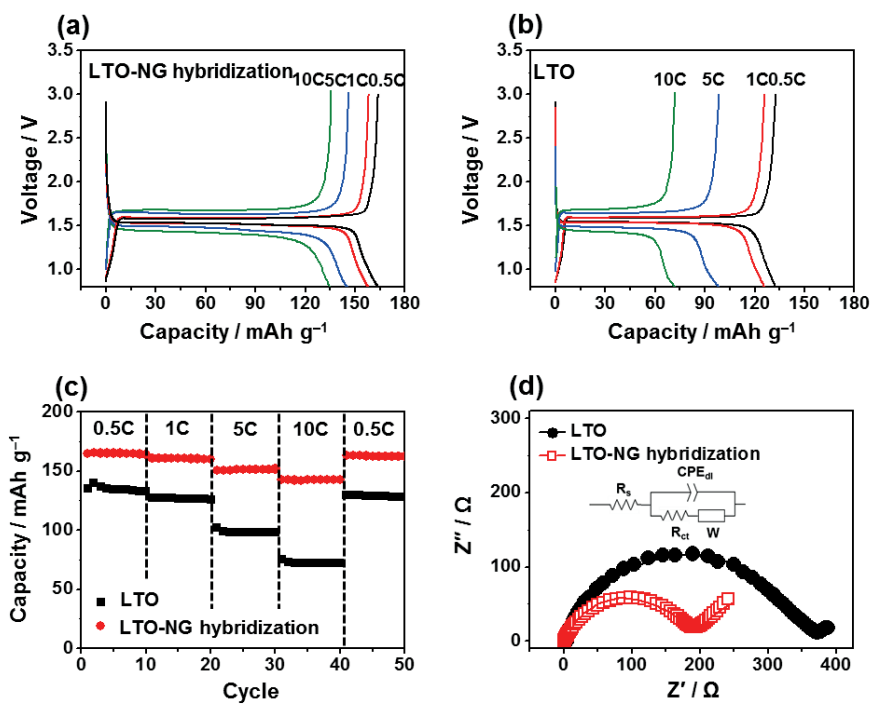


Figure 2-11. Charge-discharge profiles of (a) LTO-NG hybridization and (b) LTO electrodes at various current densities (0.5, 1, 5 and 10 C). (c) Rate capability test of LTO-NG hybridization and LTO at various current densities during each 10 cycles. (d) Nyquist plots of LTO-NG hybridization and LTO.

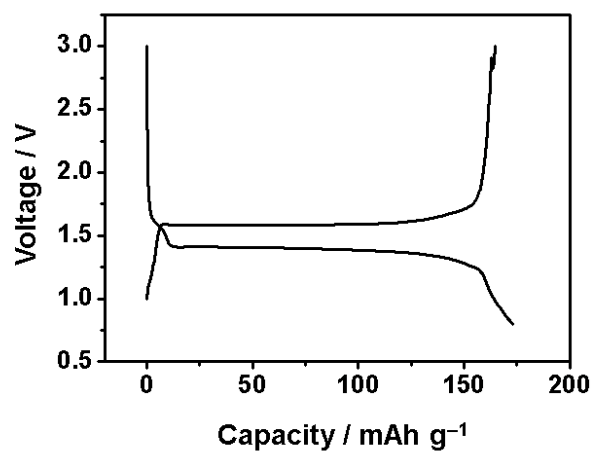


Figure 2-12. Charge/discharge profile of LTO-NG hybridization electrode at first cycle. C-rate is 0.5 C.

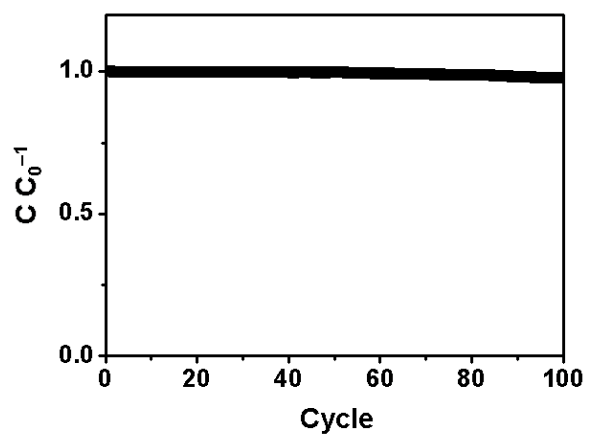


Figure 2-13. Cyclability test of LTO/NG hybridization electrode during 100 cycles. C-rate is 0.5 C.

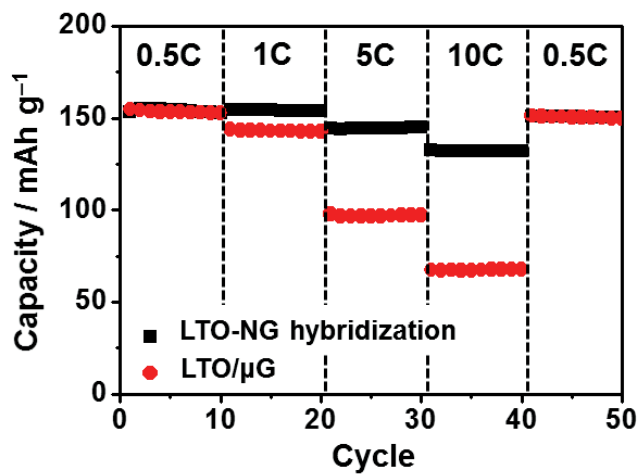


Figure 2-14. Rate capability test of LTO-NG hybridization and LTO/μG composite at various current densities during each 10 cycles.

Chapter 3. Stabilizing Discharge Products Using Electron-withdrawing Zirconia Support in Lithium-Oxygen Batteries

3.1 Introduction

Current energy density of LIBs is not satisfying the demand for the EVs [80-82]. Therefore, various next-generation battery systems have been proposed and investigated to replace the LIBs [83-85]. Lithium-sulfur, silicon and redox flow batteries are suggested as the alternative.

Among them, LOBs have extremely high energy density ($3,500 \text{ Wh kg}^{-1}$) even compared to the LIBs. Therefore LOBs attract attentions as the highly promising candidate to substitute the conventional LIB [86]. However, high overpotential and low cycle life have impeded the practical use of LOBs. One of the cause of the impediment is that the Li_2O_2 decomposition reaction during charging process is highly resistive due to the low electric conductivity of Li_2O_2 . Also, side reactions can occur on the cathode where lithium ion reacts with external oxygen resulting Li_2O_2 . Because superoxide and peroxide species (SPS,

O_2^- , LiO_2 and Li_2O_2) are not stable, it can easily react with electrolyte and carbon electrode, which result passivation of cathode and higher decomposing potential than of Li_2O_2 [39,87,88].

Various catalysts have been proposed for LOBs to solve the issues regarding high overpotential and low cycle life [89-92]. Among them, noble metal catalysts (NMCs) have shown remarkable performance due to high catalytic activity which could reduce overpotential [93-95]. However, NMCs not only catalyze the Li_2O_2 decomposition, but also promote side-reactions, because the catalytic behavior of NMCs is not selective [40,41]. Byproducts from the side-reactions increase interfacial resistance which has a negative influence on the cycling ability and causes a gradual increase in the overpotential [96-98]. Therefore, the stabilization of SPS is the key strategy for stable and reversible reactions of NMCs in LOBs.

Designing the cathode material of LOBs could be a solution to relieve the side reactions. Several types of metal oxides are known to stabilize the SPS via oxygen defects on the surface [99,100]. Because SPS are nucleophilic, they easily bind with oxygen defect sites, which could relieve their reactivity. Adaptation of the surface properties of these metal oxides is necessary to

suppress the byproduct formation. Therefore, the concept of hybridization between highly active NMCs and the SPS-stabilizing metal oxides should be pursued.

In this research, a platinum catalyst deposited onto zirconia is proposed for our proof-of-concept model to establish the synergetic effect of NMCs and oxygen-defective support. We chose zirconia as a support because it offers oxygen defect on the surface without providing additional oxygen reduction/evolution reaction site during charge/discharge. Therefore, reactions occur mainly on the platinum surface. We observed the effect of support with oxygen defect by experimental and theoretical approaches relative to the performance of LOBs. As a result, Pt/ZrO₂ exhibited longer cyclability compared to a sole platinum catalyst. The electrochemical and physicochemical properties of both catalysts and the discharged products were characterized via experimental and theoretical methods to investigate the origins of the longer cyclability. The oxygen defect site of the zirconia support improved the reversibility by interacting with discharge products.

3.2 Experimental

3.2.1 Fabrication of platinum deposited onto a zirconia support (Pt/ZrO₂)

10 wt% of platinum precursor (H₂PtCl₆·6H₂O) was added to 0.05 g ZrO₂ in 100 ml water. The solution was stirred for 1 h and sonicated for 1 h. A NaBH₄ solution (0.15g, 50ml) was slowly added drop-wise to the sample solution to reduce the platinum. The solution was aged for 12 h and washed with distilled water. The sample was dried in a 60 °C oven for 12 h. Commercial platinum black was used for the platinum catalyst for comparison.

3.2.2 Characterization

The morphology and surface properties were measured by transmitted electron microscopy (TEM, JEOL, JEM-2100), X-ray diffraction (XRD, Rigaku, D/max-2200), BET analysis (Micrometrics, ASAP2010) and X-ray spectroscopy (XPS, Thermo Scientific, Sigma Probe)

3.2.3 Electrochemical characterization

The Swagelok-type LOB cells were assembled using lithium metal as an anode, 1 M Bis(trifluoromethane) sulfonamide lithium dissolved in tetraethylene glycol dimethyl ether (TEGDME) was used as an electrolyte and gas-diffusion layer with the catalyst as a cathode. All cells were fabricated in an argon-filled glove box. Catalysts were applied via a spray gun using catalyst ink. 10 mg of catalyst was added into 5 ml 2-propanol for catalyst ink. The amount of loaded Pt/ZrO₂ was 0.5 mg cm⁻². To equalize the amount of active material without support, the mass density of Pt particle electrode was adjusted to 0.05 mg cm⁻². Before the electrochemical characterization, cells were transferred to an oxygen-filled chamber. Charge/discharge tests were conducted with a multichannel automatic battery cycler (WonATech, WBCS3000). Cyclic voltammetry and galvanostatic tests were carried out using a potentiostat (WonATech, ZIVE 2). In galvanostatic reduction/oxidation test, a three-electrode configuration was used with a glassy carbon electrode with a diameter of 5 mm as the working electrode and platinum meshes as counter and pseudo-reference electrodes. 7 μl of catalyst ink was fabricated by mixing 10 mg catalyst, 5 mg Nafion and 0.8 ml 2-propanol, which was dropped

onto a glassy carbon and dried. 0.5 M tetrabutylammonium (TBA) perchlorate dissolved in dimethyl sulfoxide (SAMCHUN chemicals) was used for the electrolyte and O₂ purge for 1h before the test.

3.2.4 Computational details

Periodic DFT calculations were conducted using a VASP. PBE exchange-correlation functional was applied to a GGA [66,67]. Ionic cores were calculated under the PAW method [68]. The energy cutoff for the plane wave basis was 520 eV. A Brillouin zone was described by 1×1×1 Monkhorst-Pack k-point mesh. DFT+U calculation was introduced with $U_{\text{eff}} = 4$ eV for zirconium. This U value was obtained from the construction of electronic and geometric structures of bulk zirconia [101]. This U_{eff} is also used to calculate the stability of zirconia nanoparticle with various shapes [102]. The van der Waals interactions are described using a DFT+D2 method established by Grimme. The source of the parameters for Grimme's potential was studied by F. Picaud [103] and G. Kresse [104].

3.3 Results and discussion

3.3.1 Characterization

To compare the morphology of Pt/ZrO₂ and Pt particle, TEM were conducted (Figure 3-1). TEM images revealed that platinum particles in similar size (less than 10 nm) and shape were dispersed uniformly onto larger (approximately 50 nm) zirconia particles for Pt/ZrO₂. Pure Pt particle are similar in size and shape to those that were deposited onto the zirconia. This suggests that the morphological differences in the active sites between Pt/ZrO₂ and Pt particles are negligible. X-ray diffraction (XRD) patterns detailed the crystallinity of Pt/ZrO₂ and Pt particles (Figure 3-2). Both samples had the same face-centered cubic crystalline platinum peaks (JCPDS, Card no. 04-0802), which can be attributed to the (111) and (200) planes. The crystal structure of zirconia was characterized as purely monoclinic (JCPDS, Card no. 37-1484). BET surface area analysis also verified that surface area effect could be ignored. The BET specific surface areas of the Pt/ZrO₂ and Pt particles were 22.6 cm² g⁻¹ and 15.1 cm² g⁻¹, respectively. Pore structures were not developed on the surfaces of either Pt/ZrO₂ or Pt particles, which indicates that prepared materials are

conventional metal oxide and metal particles (Figure 3-3).

The oxidation states of the surface atoms of Pt/ZrO₂ were characterized via XPS.

O1s, Zr3d and Pt4f orbital of Pt/ZrO₂ are described in Figure 3-4. The peak of

O1s orbital was deconvoluted into two parts, 529.8 eV and 531.7 eV. Binding

energy at 529.8 eV is associated with the oxygen ion in the lattice of zirconia.

531.7 eV is interpreted as oxygen defect or adsorbed species on the surface of

zirconia [105-107]. Physisorbed species can be easily removed by the vacuum

conditions of XPS analysis. Therefore, any observed oxygen are chemisorbed

species such as hydroxyl group or water, which bind mostly with oxygen

defects on zirconia. Therefore, the peak at 531.7 eV is directly related to oxygen

defect. The evolved peaks at 181.9/184.4 eV and 181.4/183.8 eV were assigned

as Zr⁴⁺ and Zr³⁺, respectively. Peaks of 70.3/73.7 eV (red line), 71.5/74.9 eV

(blue line) and 72.6/75.9 eV (green line) are assigned for Pt⁰, Pt²⁺ and Pt⁴⁺,

respectively.

3.3.2 Electrochemical measurement

The electrochemical performance of the Pt/ZrO₂ used as catalytic cathode for

LOB was evaluated via galvanostatic charge/discharge test at a current density

of 0.2 mA cm^{-2} , in a voltage window of 2.0–5.0 V and with a limited time of 2.5 h (cut-off capacity of $1,000 \text{ mAh g}^{-1}$) (Figure 3-5a). Electrochemical test of Pt particle was also conducted using the same condition (Figure 3-5b). At first cycle, the discharging/charging potentials of Pt/ZrO₂ and Pt were observed at 2.7/4.2 V and 2.7/3.5 V, respectively. Even the charging overpotential of Pt was relatively lower than that of Pt/ZrO₂ at initial few cycles, however, it dramatically increased from 5th cycle and the fast degradation of performance was observed near 40th cycle. In contrast, Pt/ZrO₂ maintained a flat charge profiles and a capacity even after the 40th cycle.

Since the charging potential is closely related to the oxidation of a discharge product, the low initial overpotential of the Pt particle indicates that it definitely catalyzes the oxidation reaction. However, as the cycle proceeded, both the charging potential and the variation in the potential profile were drastically worsen. As stated at the beginning, this phenomenon is due to the formation of byproducts from undesired reactions by platinum catalyst [40,41]. The Pt/ZrO₂, on the other hand, maintained its performance for longer cycles. The consistent charging profiles of Pt/ZrO₂ suggest that less byproducts were formed with Pt/ZrO₂. Based on these results, the better cyclability of the platinum with a

zirconia support can be explained by highly reversible lithium-oxygen redox chemistry without side-reactions.

3.3.3 Stability measurement of the discharge products

To investigate the effect of the zirconia as a support material for platinum catalyst, the reactivity of the intermediates and final discharge products of LOBs were investigated. Because SPS undergo nucleophilic attack with electrolytes and carbon-based electrode during charge/discharge reaction, measuring the stability of SPS could be the criterion for the reversibility of the charge/discharge reactions. Figure 3-6a shows the results of the galvanostatic reduction/oxidation test of Pt/ZrO₂ and Pt particle under 0.5 M TBA salt. Pt/ZrO₂ group exhibits higher overpotential than Pt particle due to the low conductivity of zirconia support. Because LiO₂ and Li₂O₂ cannot be formed in this condition, only O₂⁻ is observed. Even with TBA, O₂⁻ still maintains its reactivity toward electrolyte. Therefore, the amount of re-oxidized O₂⁻ is always smaller than the reduced O₂⁻, and oxygen collection efficiency indicates the side-reaction rate of O₂⁻. The ratio of a re-oxidation and reduction current (I_o/I_r) increased from 28.4% (Pt particle) to 38.5% (10 wt% Pt/ZrO₂), which implies

that O_2^- consumption is suppressed by zirconia support. Oxygen defects on the exposed surface of zirconia function as binding sites for O_2^- , which mitigates the reactivity of O_2^- . Therefore, the reaction between O_2^- and an electrolyte is diminished in Pt/ZrO₂. However, as the Pt content in Pt/ZrO₂ is increased from 10 to 20 wt%, oxygen collection efficiency was decreased to 24.7%. This is because the oxygen defects on the exposed zirconia surface and the binding sites for O_2^- were decreased as shown in Figure 3.7. As expected, the oxygen collection efficiency and cyclability of samples have the same tendency (Figure 3-6b). It is clear that the stabilization of O_2^- is a critical factor for the reversibility of a charge/discharge reaction, which defines the cyclability of LOBs.

Side-reactions also occur on the surface of the final discharge product, Li₂O₂. To investigate the reactivity of Li₂O₂ in the presence of the prepared catalysts, the LOBs with Pt/ZrO₂ and Pt particle were rested for 2 days after discharging (Figure 3-8). Without rest, the flat charging potential plateau of the Pt particle was observed at 3.5 V. After 2 days of rest, however, it was increased up to 4 V with sloped profile. 20 wt% Pt/ZrO₂, which has less exposed zirconia defect site than that of 10 wt% Pt/ZrO₂, showed the charging potential plateau at 4 V.

In contrast, after 2 days of rest, the charging potential was increased and showed sloped profile above 4 V. In contrast, the charging potentials of 10% Pt/ZrO₂ with and without a rest of 2 days were similar and flat-shaped near 4.2 V. According to the previous studies, larger amount of CO₂ gas was observed during the sloped charge region that was originated from the decomposition of Li₂CO₃, which is a byproduct [108-110]. Therefore, the appearance of a sloped charge potential curve indicates that a portion of Li₂O₂ has converted to Li₂CO₃ during the rest time. These results provide evidence that Li₂O₂ is unstable and converted into another chemical on the platinum surface, but is stable on a zirconia surface that suppresses side-reactions. As shown by the galvanostatic reduction/oxidation test results under TBA salt, zirconia support enables reversible reactions by stabilizing the intermediate and final-discharge products in LOBs.

3.3.4 Calculation of Li₂O₂ stability on the catalyst

DFT calculations were carried out to exhibit the detailed interactions of Li₂O₂ adsorbed onto platinum (111) and zirconia (-111) planes, respectively, which are the most stable and abundant facets of each compound (Figure 3-9a,b) [111,

112]. The adsorption energy of a Li_2O_2 monomer on platinum and zirconia were calculated as - 3.15 eV and -7.97 eV, respectively. The calculated values of binding energies of a dimer and a trimer also show that Li_2O_2 was adsorbed more strongly on the surface of zirconia. Since the adsorption energy of Li_2O_2 is related to its stability, the reactivity of Li_2O_2 is suppressed on the zirconia surface. The charging density difference between Li_2O_2 trimer in vacuum and Li_2O_2 trimer adsorbed onto platinum and zirconia surfaces shows the interaction of Li_2O_2 with these surfaces. The polarization of Li_2O_2 increases on the surface of platinum, which means a stronger nucleophilic attack could occur. By contrast, Li_2O_2 interacts strongly with zirconia and is stabilized by losing the electron density. As the nucleophilicity of Li_2O_2 is reduced, its reactivity toward electrolyte or electrode could be relieved. The results on the platinum (200) and zirconia (111) planes, which are the second most stable and abundant planes also showed analogous tendency (Figure 3-9c,d). Therefore, these phenomena would be general on the surfaces of platinum and zirconia.

We also calculated the solvation energy of Li_2O_2 in TEGDME electrolyte, which is calculated as 1.73 eV. Adsorption energies of both platinum and zirconia surface to lithium superoxide are stronger than solvation energy of

TEGDME to lithium superoxide. Therefore, lithium superoxide is adsorbed on the surface rather than dissolved to the electrolyte, which agrees with previous studies. In case of electrolyte with low donor number, Li_2O_2 grows on the surface of electrode without solvation of electrolyte [113,114].

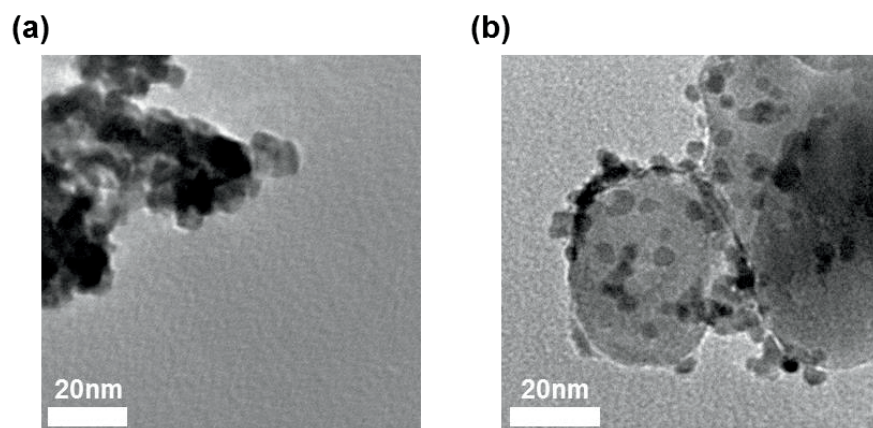


Figure 3-1. TEM image of (a) Pt particle, (b) 10 wt% Pt/ZrO₂

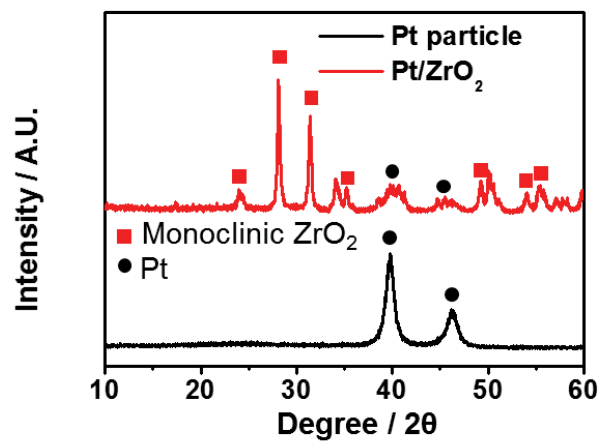


Figure 3-2. XRD patterns of Pt particle and Pt/ZrO₂.

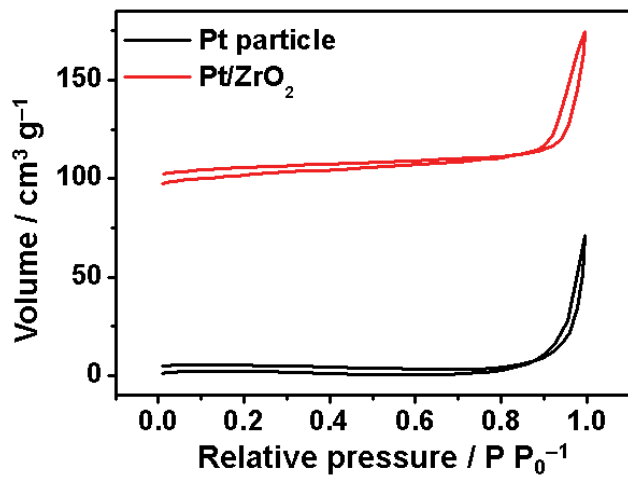


Figure 3-3. N₂ adsorption-desorption isotherms of Pt particle and Pt/ZrO₂.

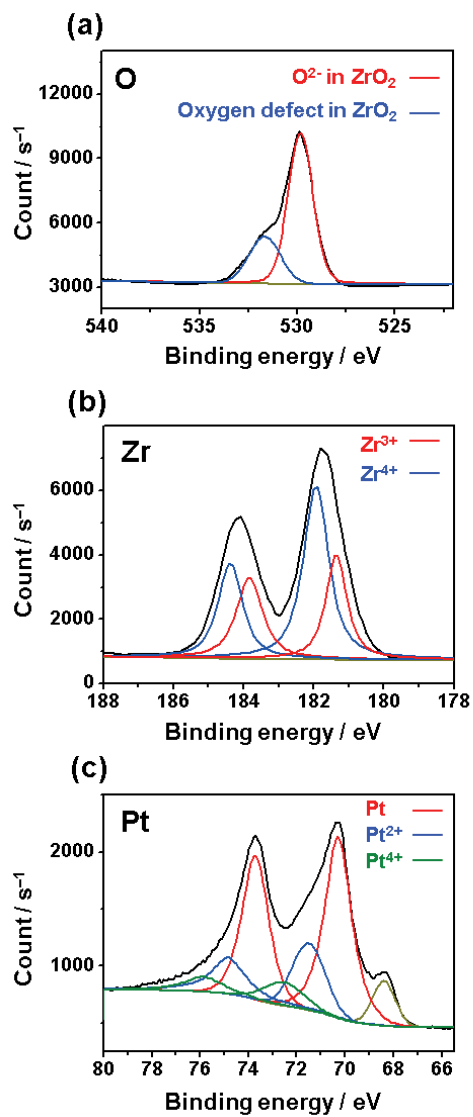


Figure 3-4. XPS spectra of (a) O1s, (b) Zr3d and (c) Pt4f orbital of Pt/ZrO₂.

Olive lines of Figure 3-4c are background.

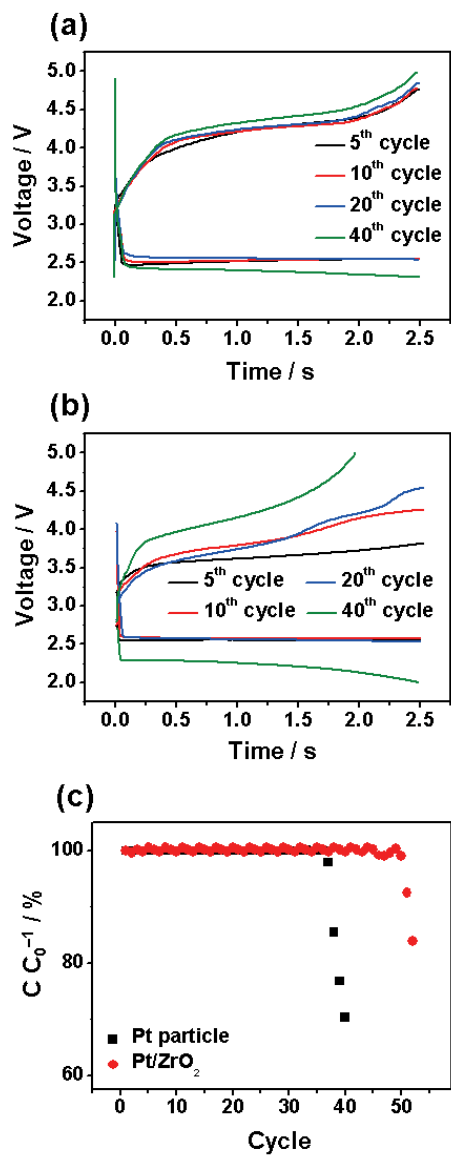


Figure 3-5. Charge/discharge profiles at 0.2 mA cm⁻² of (a) Pt/ZrO₂ and (b) Pt particle. (c) cyclability test of Pt/ZrO₂ and Pt particle at 0.2 mA cm⁻².

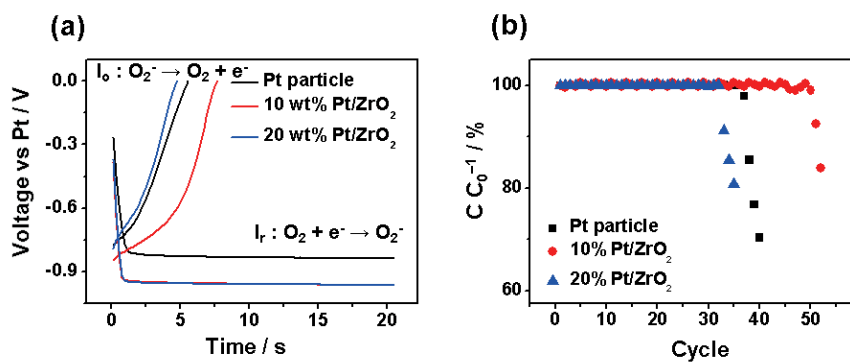


Figure 3-6. (a) Galvanostatic charge/discharge test of 10, 20 wt% Pt/ZrO₂ and Pt particle under TBA salt at 5 μA, (b) Cyclability test of 10, 20 wt% Pt/ZrO₂ and Pt particle.

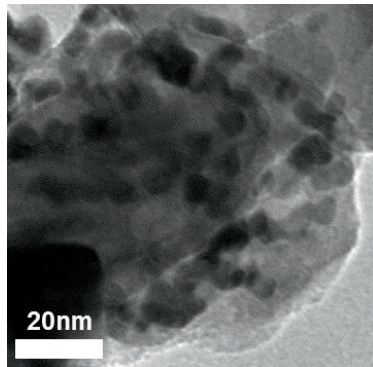


Figure 3-7. SEM image of 20 wt% Pt/ZrO₂.

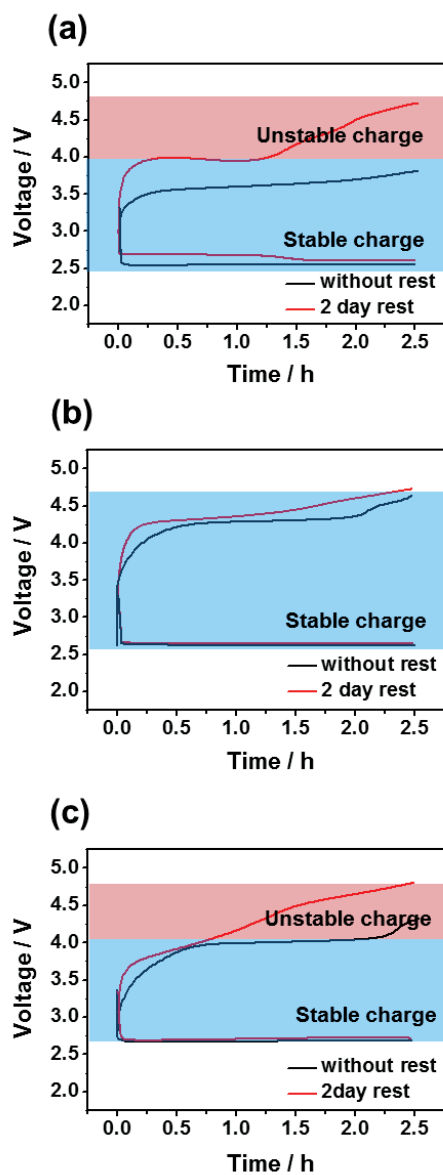


Figure 3-8. Charge/discharge profiles without rest and with 2 days rest between charge and discharge process of (a) Pt particle, (b) 10 wt% Pt/ZrO₂ and (c) 20 wt% Pt/ZrO₂.

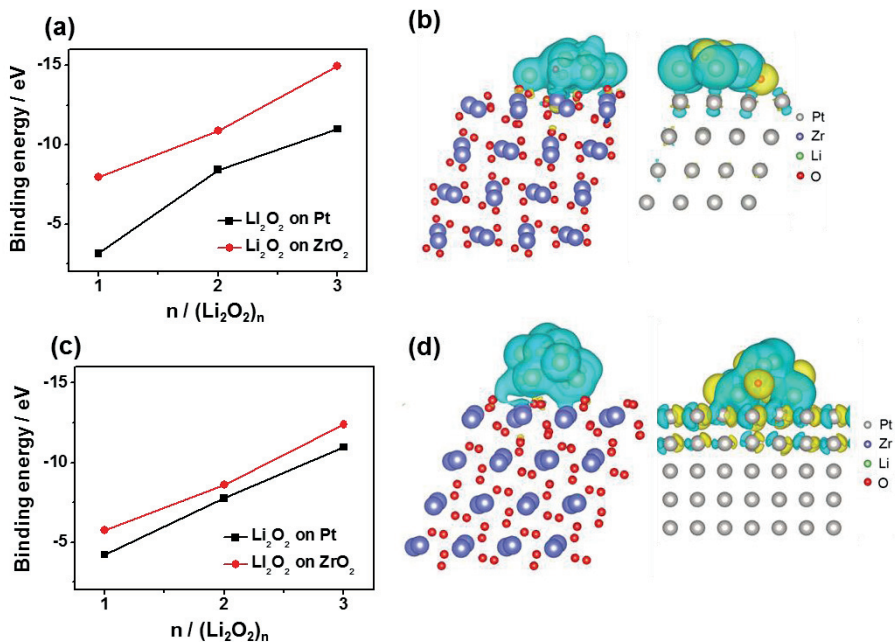


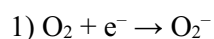
Figure 3-9. (a) Calculated binding energy of $(\text{Li}_2\text{O}_2)_n$ ($n = 1,2,3$) adsorbed on Pt (111) and ZrO_2 (-111). (b) Charge density difference of Li_2O_2 adsorbed on Pt (111) and ZrO_2 (-111). (c) Calculated binding energy of $(\text{Li}_2\text{O}_2)_n$ ($n = 1,2,3$) adsorbed on Pt (200) and ZrO_2 (111). (d) Charge density difference of Li_2O_2 adsorbed on Pt (200) and ZrO_2 (111). The isosurfaces are plotted at positive (yellow) and negative (blue) values.

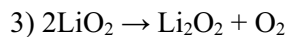
Chapter 4. Dependence of the Physicochemical Properties of Discharge Products in Lithium-Oxygen Batteries on the reaction kinetics

4.1 Introduction

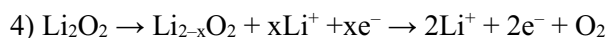
The increasing demand for high energy density energy storage systems has promoted the research of LOBs, particularly targeting electrified green vehicles that require increased mileage per charge [80-82]. The use of gas-phase active material on the cathode side is centered in boosting the energy density in comparison with conventional LIBs that rely on solid-state active phases on both sides of a cell. Whereas the motivation of developing LOBs is clear in this line, the technology generally suffers from insufficient sustainability over long-term cycling [34,5]. While the main reaction involving the following three steps is well-accepted, a variety of parasitic reactions are not completely under control [32,33].

Discharge





Charge



A representative strategy to enhance the reversibility in each discharge-charge cycle is to adopt OER catalysts since charging process consists of oxygen evolution [40-45]. In practice, the efficiency and sustainability of a catalyst are influenced by various reaction conditions, such as mass transfer, beside the intrinsic material properties of the catalyst. In this vein, the geometry and dimensions of a catalyst's substrate could play a role [115,116]. According to the overall reaction scheme above, Li_2O_2 is the final product reached at the end of the discharge. However, the progression of reaction (3) might be varied depending on the reaction condition so that the efficiency of the overall reaction (or charge/discharge overpotential) could be different because LiO_2 , the intermediate product, holds higher electronic conductivity than that of Li_2O_2 [35,117]. It was recently found that discharge product can contain remaining LiO_2 -like species and iridium catalyst can stabilize LiO_2 to improve the reaction reversibility, although the progression of reaction (3) is still difficult to control

in most cases [48,118]. Similarly, the current investigation reports that the pore size of a carbon substrate has a clear effect on the preference between LiO_2 and Li_2O_2 during the course of the reaction. This rationale is related to the fact that the pore size of a substrate determines the diffusivity of the reactants, which subsequently affects the reaction kinetics. Direct comparison between small and large pore catalysts (SPC and LPC) reveal that the large one slows down the formation of insulative Li_2O_2 and promotes the preservation of LiO_2 -like species, improving the reversibility.

4.2 Experimental

4.2.1 Preparation of porous carbon catalyst

A silica template was fabricated via modification of a procedure established in a study by Polshettiwar et al [119]. 2.5 g tetraethyl orthosilicate in 30 ml cyclohexane with 1 ml (for SPC) or 2.5 ml (for LPC) 1-pentanol solution was mixed with 1 g cetylpyridinium bromide hydrate, 0.6 g urea in 30 ml D. I. water solution. The method used to prepare the porous carbons with this template was described in previous work [120]. Etching step of silica was not proceeded in order to effectively maintain its structure.

4.2.2 Characterization

The morphologies of materials were observed via SEM (Carl Zeiss, SUPRA 55VP), XRD (Rigaku, D/max-2200) and BET analysis (Micrometrics, ASAP2010).

4.2.3 Electrochemical characterization

Cathode electrode was prepared by spraying the fabricated sample onto

carbon paper with a loading density of 0.5 mg cm^{-2} . A Swagelok-type LOB cell was assembled with a cathode, glass fiber separator, lithium foil anode, and 1M LiNO_3 /dimethyl sulfoxide (DMSO) electrolyte. Charge/discharge test was conducted with a multichannel automatic battery cycler (WonATech, WBCS3000), and EIS was conducted using a potentiostat (WonATech, ZIVE 2).

4.3 Results and discussion

4.3.1 Characterization

Figure 4-1 shows the SEM images and BET surface area analyses of SPC and LPC. In SEM images, SPC and LPC show a wrinkled sphere shape with similar particle sizes of approximately 200 to 300 nm, but SPC has denser and smaller pores. Although characteristic peaks of graphite occurred on XRD patterns, crystallinity of SPC and LPC is amorphous because the peak width of graphite is too broad (Figure 4-2). The N₂ adsorption/desorption isotherms of both catalysts demonstrate the same type-2 behavior, which indicates that SPC and LPC are both macroporous. The surface areas of SPC and LPC are measured as 131.4 m² g⁻¹ and 155.5 m² g⁻¹, respectively. No remarkable difference is detected in the surface of the two catalysts, however, pore size analysis indicates that LPC (135 nm) has four-fold larger pore than that of SPC (35 nm).

4.3.2 Morphology and kinetics analysis of the discharge product

To investigate the phenomena of each electrode during charge/discharge, SEM images are obtained for SPC and LPC at indicated point during cycle (Figure

4-3 and 4-4). After the discharge, both electrodes exhibit film-type and particle-type discharge product. It is reported that there are two plateau on the charge process and two discharge product exists: LiO_2 -like species and Li_2O_2 [118]. After charge process to the point between first and second plateau, film-type discharge product is disappeared. According to Raman spectra, film-type discharge product is LiO_2 -like species (Figure 4-5). Raman spectrum of SPC electrode exhibits peak for LiO_2 and Li_2O_2 after discharge. After charge process to the point between first and second plateau, only Li_2O_2 peak is observed and LiO_2 peak disappears. At this point, smooth surface of Li_2O_2 is changed to overlapped disk because a few amount of amorphous Li_2O_2 exists on the surface [32]. Because amorphous Li_2O_2 is decomposed at the lower voltage, the surface decomposes with LiO_2 -like species. Interestingly, at the first stage of discharge (100mAh g^{-1}) only LiO_2 -like species are observed (Figure 4-3a,4-4a). It is plausible that LiO_2 -like species are converted to Li_2O_2 during discharge. Considering that solvent with high donicity like DMSO can dissolve the LiO_2 and the location of LiO_2 -like species and Li_2O_2 is different, LiO_2 -like species were dissolved in the electrolyte and recrystallized to the Li_2O_2 .

Figure 4-6 shows the rate capability test of SPC and LPC. The portion of first

plateau for SPC decreases with the current density decreases because longer reaction time indicates larger amount of Li_2O_2 . In contrast, the portion of first plateau for LPC at low current rate is almost same. To investigate this phenomena, the graphs of rate capability test are redraw to degradation of LiO_2 -like species with respect to time (Figure 4-6c). The conversion reaction from LiO_2 -like species to Li_2O_2 is the first order reaction [118]. Although the profile of SPC is well fitted with the first order reaction, the degradation rate of LPC is slower than expectation. Due to the morphological difference between SPC and LPC, growing process of LiO_2 -like species is different to each other. LiO_2 -like species on LPC exists inside the pore, however, LiO_2 -like species on SPC exists on the surface, because the pore size of SPC is not large enough to grow LiO_2 -like species. As LiO_2 -like species in the pore cannot contact with electrolyte with discharge progressing, dissolution is inhibited and the formation of Li_2O_2 becomes slow. Therefore, the portion of the first plateau of LPC is larger than that of SPC.

4.3.2 Electrochemical measurement

The galvanostatic charge/discharge profiles within a current density of 400

mA g⁻¹ are displayed in Figure 4-7. During charge process, not all of the electrons are used to oxidize the lithium compound [33,38]. Decomposition of electrolyte can also occur during charge process and some solid are remained on the surface. XRD patterns of SPC and LPC electrodes after 40 cycles shows that residues are Li₂CO₃, because Li₂CO₃ is decomposed at higher voltage than Li₂O₂ (Figure 4-8). Although both SPC and LPC are covered by Li₂CO₃, the pore structure of LPC is still maintained, while the many of pores of SPC are blocked (Figure 4-9). Therefore, LiO₂-like species of SPC are exposed on the electrolyte more easily. As a result, the capacity partition of the second plateau for SPC increases as the charge/discharge proceeds faster and LPC has less parasitic reactions due to the low overpotential of LiO₂-like species. LPC exhibits a longer cycling ability of 64 cycles compared to SPC (45 cycles).

To observe the change of resistive factor on the surface of the catalysts during cycle, EIS was conducted to the electrodes after 40 cycles. Figure 4-10 displays Nyquist plot of SPC and LPC electrodes. The equivalent circuit for the pristine SPC and LPC is described in Fig. 6c, where R_s is the ohmic resistance, R₁ and C₁ are the resistance and CPE for the cathode, and R₂ and C₂ are the resistance and CPE for the diffusion. After 40 cycles, one more parallel resistance and

CPE (R3 and C3) are added on the equivalent circuit. During cycles, lithium anode reacts with electrolyte, oxygen and by-products. As a result, conductive lithium anode is covered by lithium compound like LiOH, which causes high resistance. Therefore, R3 and C3 values are the elements for the anode. The R1 value increases with the cycles as the Li_2CO_3 passivates the surface of the catalyst. The R1 of SPC electrode after 40 cycles represents a 36-times increase (1714 Ω) compared to the R1 of pristine electrode (47 Ω). By contrast, the R1 of LPC after 40 cycles represents an increase from 99 Ω to 130 Ω . Due to the high reversibility of LPC, less parasitic reaction occurs during cycles. In addition, severe pore clogging of SPC decreases the surface area, which leads to high current density, promoting the parasitic reactions. By the same reason, R3 of SPC is 9-times larger than R3 of LPC. Rapid increase of ohmic resistance of SPC is also arisen by high resistance of anode and cathode. These phenomena indicate that a small pore structure is vulnerable to the occurrence of irreversible parasitic reaction.

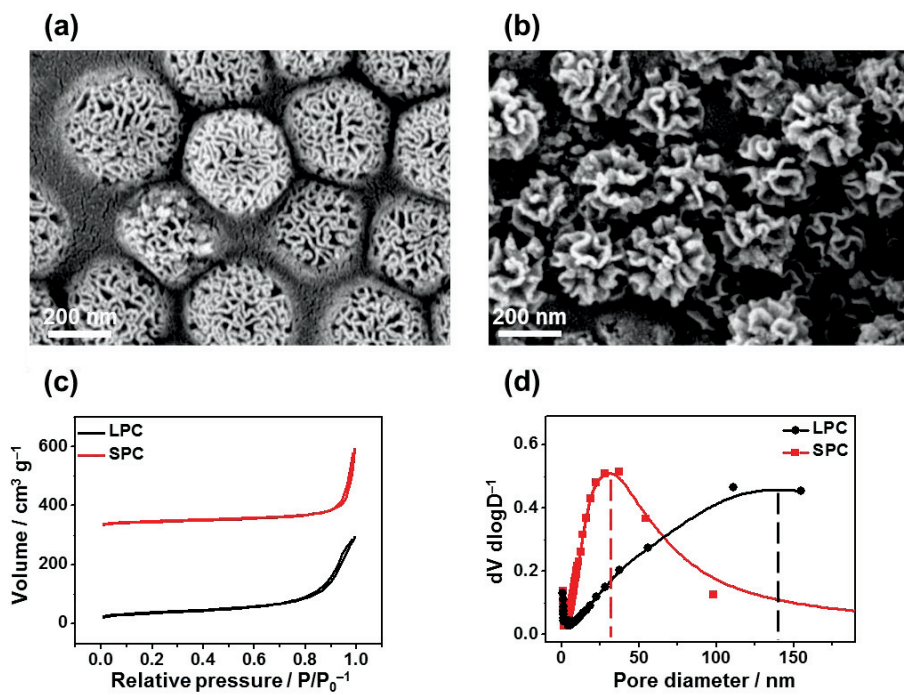


Figure 4-1. SEM images of (a) SPC and (b) LPC. (c) Pore size distributions and (d) N₂ adsorption/desorption isotherms of SPC and LPC.

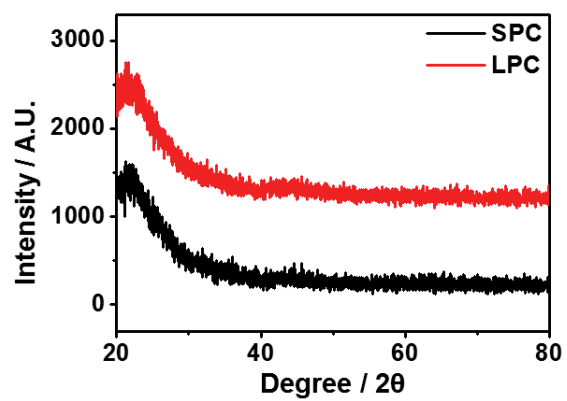


Figure 4-2. XRD patterns of SPC and LPC.

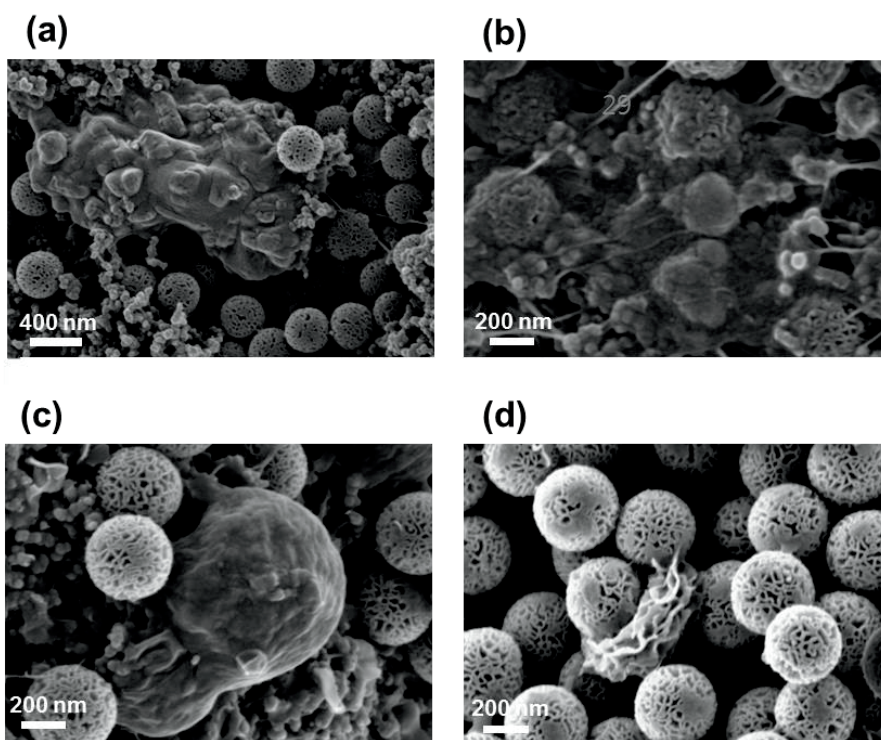
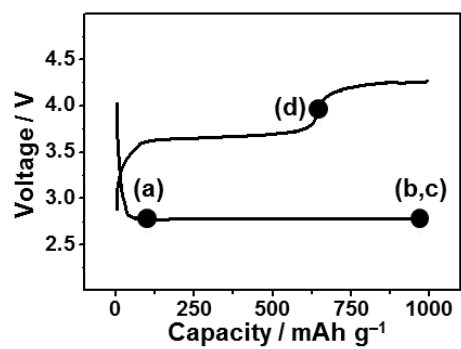


Figure 4-3. SEM images of discharged SPC electrodes at the indicated capacities (a) 100 mAh g⁻¹ and (b,c) 1000 mAh g⁻¹ and (d) charged to 4 V electrode.

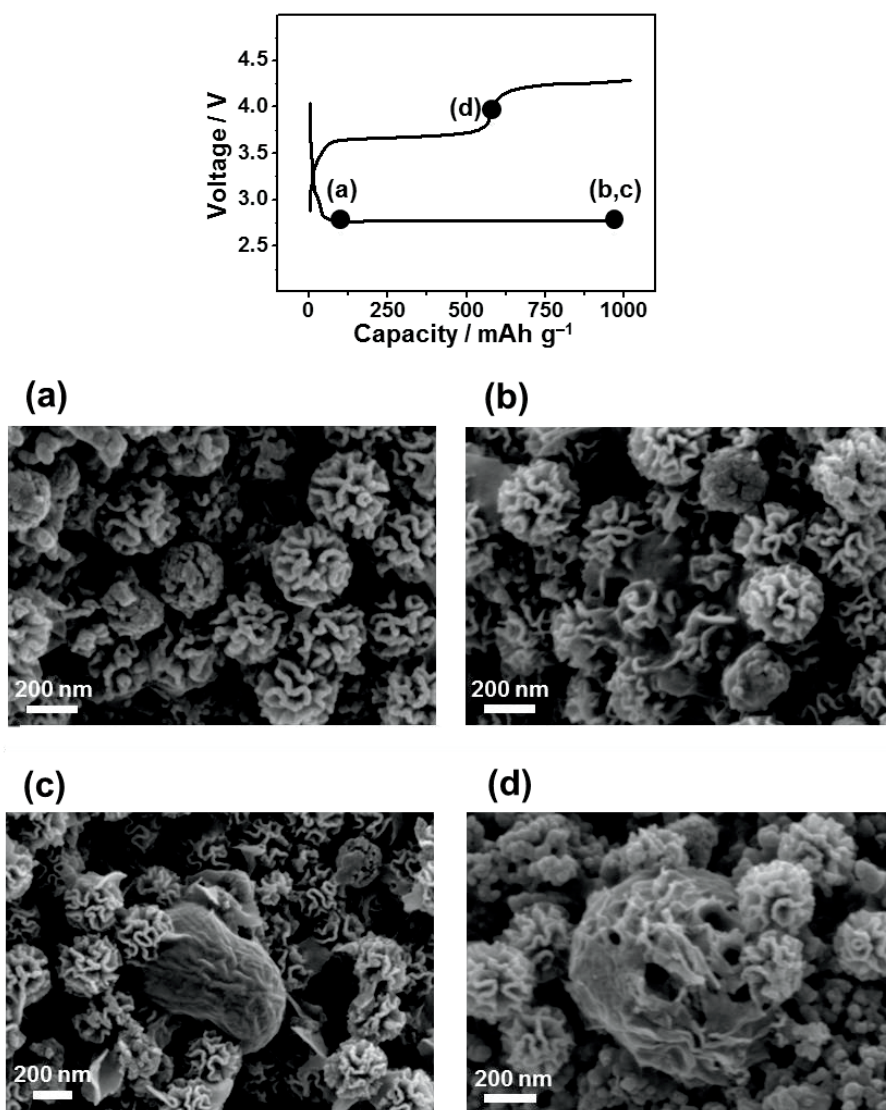


Figure 4-4. SEM images of discharged LPC electrodes at the indicated capacities (a) 100 mAh g⁻¹ and (b,c) 1000 mAh g⁻¹ and (d) charged to 4 V electrode.

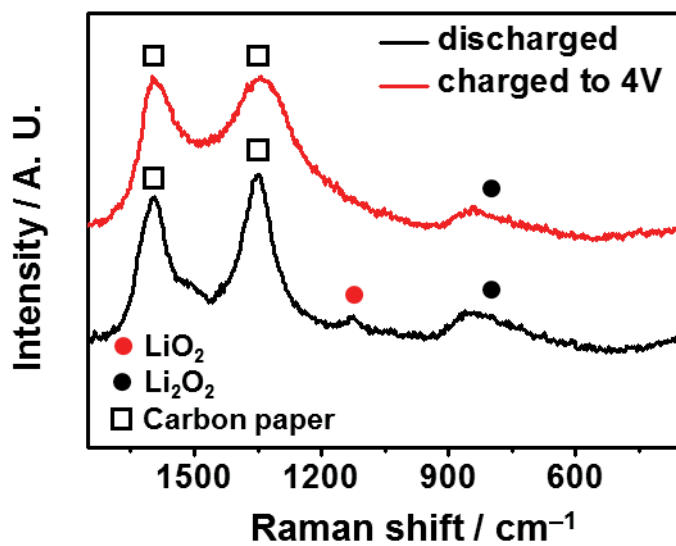


Figure 4-5. Raman spectra of discharged and charged to 4V SPC electrodes.

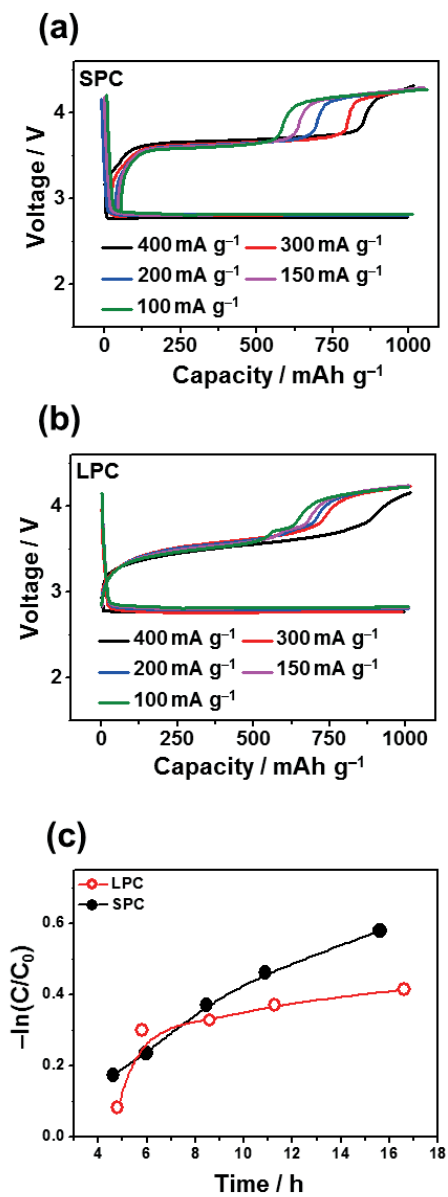


Figure 4-6. Rate capability test of (a) SPC and (b) LPC. (c) The degradation of LiO_2 with respect to time.

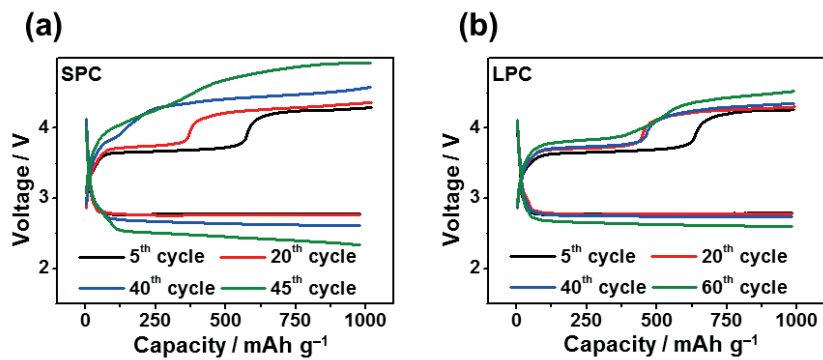


Figure 4-7. Charge/discharge profiles of (a) SPC and (b) LPC with a limited capacity of 1000 mAh g⁻¹. The current density is 400 mA g⁻¹.

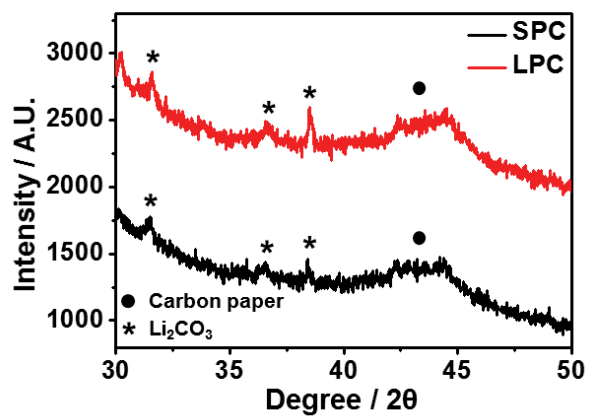


Figure 4-8. XRD patterns of SPC and LPC electrodes after 40 cycles.

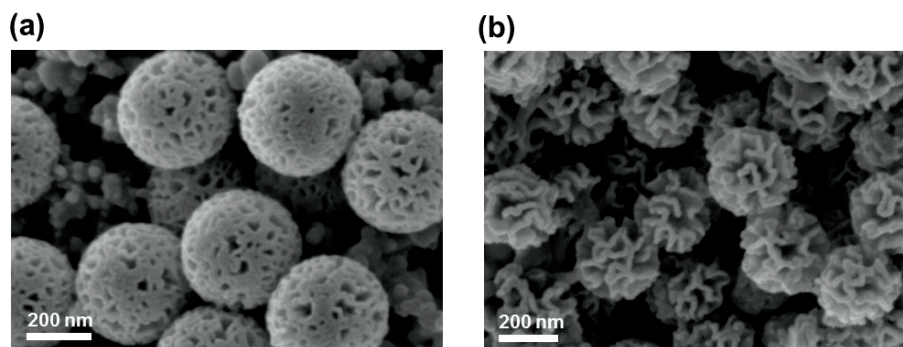


Figure 4-9. SEM images of (a) SPC and (b) LPC after 40 cycles.

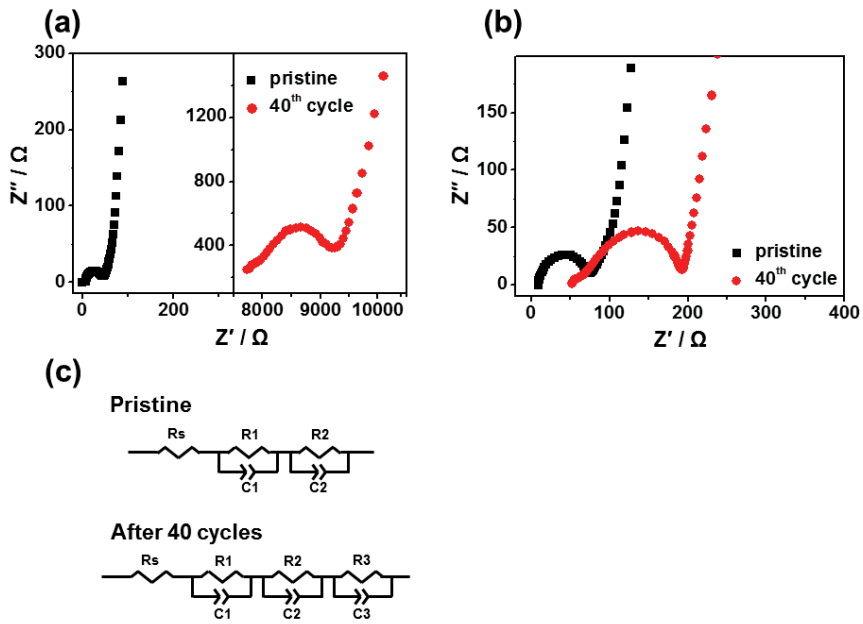


Figure 4-10. Nyquist plots of (a) SPC and (b) LPC electrodes before and after 40 cycles. (c) Equivalent circuits for pristine electrode and cycled electrode.

Chapter 5. Summary and Conclusions

As one of the strategies for the safe LIBs, graphene surrounded LTO for the anode is proposed in chapter 2. Preparation of LTO-NG hybridization by interfacial adsorption using an amphipathic solvent and a redox coupling reaction is reported. The LTO-NG hybridization exhibited a higher reversible capacity and improved rate performance compared to conventional LTO anode because of good electrical properties of the graphene-surrounding structure. Versatility of the methodology could also be applied to the preparation of other materials that require uniform graphene deposition.

For the batteries with high energy density, LOBs are studied as the next-generation battery system to overcome the conventional LIB system. To understand the mechanism of LOBs and develop the cathode catalyst with an excellent performance, two proof-of-concept researches were studied.

- Zirconia support establishes the effect of oxygen-defective and electron-withdrawing sites for a reversible charge/discharge reaction in LOBs (Chapter 3). Because nucleophilic species are stabilized on zirconia, the parasitic reactions are suppressed. As a result, platinum deposited on

zirconia demonstrated an enhanced cyclability compared to those of pure platinum catalyst. This study may offer the clues for the cathode catalyst with the reversible charge/discharge in LOBs.

- Investigation of the morphology and the growth mechanism of the discharge products in LOBs are conducted in Chapter 4. Based on the result, we revealed that the structure of cathode affects the kinetics of LOBs without metal or metal oxide catalyst. Controlling the contact between the electrolyte and the discharge product is possible by the morphological factor of the cathode catalyst, results in the modulation of the discharge product composition. Porous carbon which blocks the contact between the electrolyte and the discharge products, exhibits a low overpotential and good cyclability because the discharge product with a low overpotential is not converted to the discharge product with a high overpotential. This result could provide guideline to designing the structure of the catalytic cathode materials in LOBs.

Chapter 6. Recommendations for Further

Research

The recommendations for further research are summarized as follow;

- 1) The condition for LTO-NG hybridization is intensively studied in this dissertation. Although the improved conductivity of LTO-NG hybridization increases the rate capability of LTO in Chapter 2, optimized LTO-NG core-shell structure is required for the practical application of LTO. Therefore, it is necessary to evaluate the amphipathic solvent and graphene precursor for the solvothermal process. The methodology to obtain monolayer graphene shell should be investigated.
- 2) Cathode support material and cathode with optimized morphology are discussed in Chapter 3, 4. However, the effect of catalyst is not considered in this dissertation. The performance of LOB cathode can be increased by further upgrades with the studies on catalyst material. Catalyst which decrease the activation energy and stabilize the discharge products should be studied through the mechanistic study

and theoretical approaches. Furthermore, hybridization of the researches about support, cathode morphology and catalyst would provide optimized electrode structure for LOB catalyst.

Bibliography

- [1] J.M. Tarascon, M. Armand, *Nature*, **2001**, 414, 359-367.
- [2] M. Li, J. Lu, Z.W. Chen, K. Amine, *Adv Mater*, **2018**, 30.
- [3] F. Orsini, A. du Pasquier, B. Beaudouin, J.M. Tarascon, M. Trentin, N. Langenhuizen, E. de Beer, P. Notten, *J Power Sources*, **1999**, 81, 918-921.
- [4] R. Bhattacharyya, B. Key, H.L. Chen, A.S. Best, A.F. Hollenkamp, C.P. Grey, *Nat Mater*, **2010**, 9, 504-510.
- [5] D.W. Murphy, F.J. Disalvo, J.N. Carides, J.V. Waszczak, *Mater Res Bull*, **1978**, 13, 1395-1402.
- [6] M. Lazzari, B. Scrosati, *J Electrochem Soc*, **1980**, 127, 773-774.
- [7] A.N. Dey, *J Electrochem Soc*, **1971**, 118, 1547-1549.
- [8] J.O. Besenhard, *J Electroanal Chem*, **1978**, 94, 77-81.
- [9] M.M. Thackeray, P.J. Johnson, L.A. Depicciotto, P.G. Bruce, J.B. Goodenough, *Mater Res Bull*, **1984**, 19, 179-187.
- [10] C. Shen, G.H. Hu, L.Z. Cheong, S.Q. Huang, J.G. Zhang, D.Y. Wang, *Small Methods*, **2018**, 2.
- [11] L.X. Kong, Y.J. Xing, M.G. Pecht, *Ieee Access*, **2018**, 6, 8387-8393.
- [12] B. Diouf, R. Pode, *Renew Energ*, **2015**, 76, 375-380.
- [13] M.R. Palacin, A. de Guibert, *Science*, **2016**, 351.
- [14] R. Schmuch, R. Wagner, G. Horpel, T. Placke, M. Winter, *Nat Energy*, **2018**, 3, 267-278.
- [15] T. Yuan, Z.P. Tan, C.R. Ma, J.H. Yang, Z.F. Ma, S.Y. Zheng, *Adv Energy Mater*, **2017**, 7.
- [16] B.T. Zhao, X. Deng, R. Ran, M.L. Liu, Z.P. Shao, *Adv Energy Mater*, **2016**, 6.
- [17] C. Wang, S. Wang, L.K. Tang, Y.B. He, L. Gan, J. Li, H.D. Du, B.H. Li, Z.Q. Lin, F.Y. Kang, *Nano Energy*, **2016**, 21, 133-144.

- [18] J. Wang, H.L. Zhao, Z.L. Li, Y.T. Wen, Q. Xia, Y. Zhang, G. Yushin, *Adv Mater Interfaces*, **2016**, 3.
- [19] Y. Zhang, H. Dong, H. Zhang, Y.J. Liu, M.D. Ji, Y.L. Xu, Q.Q. Wang, L. Luo, *Electrochim Acta*, **2016**, 201, 179-186.
- [20] F. Gu, G. Chen, *Int J Electrochem Sc*, **2012**, 7, 6168-6179.
- [21] X.C. Sun, P.V. Radovanovic, B. Cui, *New J Chem*, **2015**, 39, 38-63.
- [22] S. Mao, X.K. Huang, J.B. Chang, S.M. Cui, G.H. Zhou, J.H. Chen, *Npg Asia Mater*, **2015**, 7.
- [23] Y.X. Tang, Y.Y. Zhang, X.H. Rui, D.P. Qi, Y.F. Luo, W.R. Leow, S. Chen, J. Guo, J.Q. Wei, W.L. Li, J.Y. Deng, Y.K. Lai, B. Ma, X.D. Chen, *Adv Mater*, **2016**, 28, 1567-1576.
- [24] Y. Oh, S. Nam, S. Wi, J. Kang, T. Hwang, S. Lee, H.H. Park, J. Cabana, C. Kim, B. Park, *J Mater Chem A*, **2014**, 2, 2023-2027.
- [25] G.K. Wang, C.X. Lu, X. Zhang, B.A. Wan, H.Y. Liu, M.R. Xia, H.Y. Gou, G.Q. Xin, J. Lian, Y.G. Zhang, *Nano Energy*, **2017**, 36, 46-57.
- [26] H. Yan, W. Yao, R.Z. Fan, Y. Zhang, J.H. Luo, J.G. Xu, *Acs Sustain Chem Eng*, **2018**, 6, 11360-11366.
- [27] W. Kempton, *Nat Energy*, **2016**, 1.
- [28] Z.P. Cano, D. Banham, S.Y. Ye, A. Hintennach, J. Lu, M. Fowler, Z.W. Chen, *Nat Energy*, **2018**, 3, 279-289.
- [29] A. Fotouhi, D.J. Auger, K. Propp, S. Longo, M. Wild, *Renew Sust Energ Rev*, **2016**, 56, 1008-1021.
- [30] X.W. Gao, Y.H. Chen, L.R. Johnson, Z.P. Jovanov, P.G. Bruce, *Nat Energy*, **2017**, 2.
- [31] Y.B. Yin, X.Y. Yang, Z.W. Chang, Y.H. Zhu, T. Liu, J.M. Yan, Q. Jiang, *Adv Mater*, **2018**, 30.
- [32] S. Ganapathy, B.D. Adams, G. Stenou, M.S. Anastasaki, K. Goubitz, X.F. Miao, L.F. Nazar, M. Wagemaker, *J Am Chem Soc*, **2014**, 136, 16335-16344.

- [33] N. Mahne, O. Fontaine, M.O. Thotiyl, M. Wilkening, S.A. Freunberger, *Chem Sci*, **2017**, 8, 6716-6729.
- [34] C.V. Amanchukwu, J.R. Harding, Y. Shao-Horn, P.T. Hammond, *Chem Mater*, **2015**, 27, 550-561.
- [35] W.J. Kwak, J.B. Park, H.G. Jung, Y.K. Sun, *Acs Energy Lett*, **2017**, 2, 2756-2760.
- [36] J. Lu, K. Amine, *Energies*, **2013**, 6, 6016-6044.
- [37] C. Ling, R.G. Zhang, K. Takechi, F. Mizuno, *J Phys Chem C*, **2014**, 118, 26591-26598.
- [38] B.D. Adams, R. Black, Z. Williams, R. Fernandes, M. Cuisinier, E.J. Berg, P. Novak, G.K. Murphy, L.F. Nazar, *Adv Energy Mater*, **2015**, 5.
- [39] X.H. Yao, Q. Dong, Q.M. Cheng, D.W. Wang, *Angew Chem Int Edit*, **2016**, 55, 11344-11353.
- [40] Y.S. Jeong, J.B. Park, H.G. Jung, J. Kirn, X.Y. Luo, J. Lu, L. Curtiss, K. Amine, Y.K. Sun, B. Scrosati, Y.J. Lee, *Nano Lett*, **2015**, 15, 4261-4268.
- [41] S.C. Ma, Y. Wu, J.W. Wang, Y.L. Zhang, Y.T. Zhang, X.X. Yan, Y. Wei, P. Liu, J.P. Wang, K.L. Jiang, S.S. Fan, Y. Xu, Z.Q. Peng, *Nano Lett*, **2015**, 15, 8084-8090.
- [42] B. Liu, P.F. Yan, W. Xu, J.M. Zheng, Y. He, L.L. Luo, M.E. Bowden, C.M. Wang, J.G. Zhang, *Nano Lett*, **2016**, 16, 4932-4939.
- [43] T.S. Kim, G.H. Lee, S. Lee, Y.S. Choi, J.C. Kim, H.J. Song, D.W. Kim, *Npg Asia Mater*, **2017**, 9.
- [44] B.G. Kim, C. Jo, J. Shin, Y. Mun, J. Lee, J.W. Choi, *Acs Nano*, **2017**, 11, 1736-1746.
- [45] K.R. Yoon, K. Shin, J. Park, S.H. Cho, C. Kim, J.W. Jung, J.Y. Cheong, H.R. Byon, H.M. Lee, I.D. Kim, *Acs Nano*, **2018**, 12, 128-139.

- [46] X.D. Lin, R.M. Yuan, S.R. Cai, Y.H. Jiang, J. Lei, S.G. Liu, Q.H. Wu, H.G. Liao, M.S. Zheng, Q.F. Dong, *Adv Energy Mater*, **2018**, 8.
- [47] A.J. Hu, J.P. Long, C.Z. Shu, R.X. Liang, J.B. Li, *Acs Appl Mater Inter*, **2018**, 10, 34077-34086.
- [48] J. Lu, Y.J. Lee, X.Y. Luo, K.C. Lau, M. Asadi, H.H. Wang, S. Brombosz, J.G. Wen, D.Y. Zhai, Z.H. Chen, D.J. Miller, Y.S. Jeong, J.B. Park, Z.Z. Fang, B. Kumar, A. Salehi-Khojin, Y.K. Sun, L.A. Curtiss, K. Amine, *Nature*, **2016**, 529, 377-382.
- [49] C. Xia, C.Y. Kwok, L.F. Nazar, *Science*, **2018**, 361, 777-781.
- [50] N. Mahne, B. Schafzahl, C. Leypold, M. Leypold, S. Grumm, A. Leitgeb, G.A. Strohmeier, M. Wilkening, O. Fontaine, D. Kramer, C. Slugovc, S.M. Borisov, S.A. Freunberger, *Nat Energy*, **2017**, 2.
- [51] M. Wagemaker, E.R.H. van Eck, A.P.M. Kentgens, F.M. Mulder, *J Phys Chem B*, **2009**, 113, 224-230.
- [52] X. Lu, L. Zhao, X.Q. He, R.J. Xiao, L. Gu, Y.S. Hu, H. Li, Z.X. Wang, X.F. Duan, L.Q. Chen, J. Maier, Y. Ikuhara, *Adv Mater*, **2012**, 24, 3233-3238.
- [53] C.Y. Ouyang, Z.Y. Zhong, M.S. Lei, *Electrochem Commun*, **2007**, 9, 1107-1112.
- [54] K.S. Park, A. Benayad, D.J. Kang, S.G. Doo, *J Am Chem Soc*, **2008**, 130, 14930-14931.
- [55] W.J.H. Borghols, M. Wagemaker, U. Lafont, E.M. Kelder, F.M. Mulder, *J Am Chem Soc*, **2009**, 131, 17786-17792.
- [56] A. Nugroho, S.J. Kim, K.Y. Chung, B.W. Cho, Y.W. Lee, J. Kim, *Electrochem Commun*, **2011**, 13, 650-653.
- [57] H. Song, S.W. Yun, H.H. Chun, M.G. Kim, K.Y. Chung, H.S. Kim, B.W. Cho, Y.T. Kim, *Energ Environ Sci*, **2012**, 5, 9903-9913.
- [58] H. Song, T.G. Jeong, Y.H. Moon, H.H. Chun, K.Y. Chung, H.S. Kim, B.W. Cho, Y.T. Kim, *Sci Rep-Uk*, **2014**, 4.

- [59] H.G. Jung, S.T. Myung, C.S. Yoon, S.B. Son, K.H. Oh, K. Amine, B. Scrosati, Y.K. Sun, *Energ Environ Sci*, **2011**, 4, 1345-1351.
- [60] H.X. Chang, H.K. Wu, *Energ Environ Sci*, **2013**, 6, 3483-3507.
- [61] W.W. Sun, Y. Wang, *Nanoscale*, **2014**, 6, 11528-11552.
- [62] H.L. Wang, L.F. Cui, Y.A. Yang, H.S. Casalongue, J.T. Robinson, Y.Y. Liang, Y. Cui, H.J. Dai, *J Am Chem Soc*, **2010**, 132, 13978-13980.
- [63] Z.S. Wu, W.C. Ren, L. Wen, L.B. Gao, J.P. Zhao, Z.P. Chen, G.M. Zhou, F. Li, H.M. Cheng, *Acs Nano*, **2010**, 4, 3187-3194.
- [64] H.L. Wang, Y. Yang, Y.Y. Liang, J.T. Robinson, Y.G. Li, A. Jackson, Y. Cui, H.J. Dai, *Nano Lett*, **2011**, 11, 2644-2647.
- [65] D.C. Marcano, D.V. Kosynkin, J.M. Berlin, A. Sinitskii, Z.Z. Sun, A.S. Slesarev, L.B. Alemany, W. Lu, J.M. Tour, *Acs Nano*, **2018**, 12, 2078-2078.
- [66] G. Kresse, J. Furthmuller, *Phys Rev B*, **1996**, 54, 11169-11186.
- [67] J.P. Perdew, K. Burke, M. Ernzerhof, *Phys Rev Lett*, **1996**, 77, 3865-3868.
- [68] P.E. Blochl, *Phys Rev B*, **1994**, 50, 17953-17979.
- [69] S. Grimme, *J Comput Chem*, **2006**, 27, 1787-1799.
- [70] L. Wang, T. Maxisch, G. Ceder, *Phys Rev B*, **2006**, 73.
- [71] J. Joo, H.B. Na, T. Yu, J.H. Yu, Y.W. Kim, F.X. Wu, J.Z. Zhang, T. Hyeon, *J Am Chem Soc*, **2003**, 125, 11100-11105.
- [72] S.G. Kwon, T. Hyeon, *Small*, **2011**, 7, 2685-2702.
- [73] Z.J. Ding, L. Zhao, L.M. Suo, Y. Jiao, S. Meng, Y.S. Hu, Z.X. Wang, L.Q. Chen, *Phys Chem Chem Phys*, **2011**, 13, 15127-15133.
- [74] S. Ganapathy, M. Wagemaker, *Acs Nano*, **2012**, 6, 8702-8712.
- [75] M. Kitta, T. Matsuda, Y. Maeda, T. Akita, S. Tanaka, Y. Kido, M. Kohyama, *Surf Sci*, **2014**, 619, 5-9.
- [76] H.I. Kim, G.H. Moon, D. Monllor-Satoca, Y. Park, W. Choi, *J Phys Chem C*, **2012**, 116, 1535-1543.

- [77] S. Yu, H.J. Yun, Y.H. Kim, J. Yi, *Appl Catal B-Environ*, **2014**, 144, 893-899.
- [78] S. Hoang, S.P. Berglund, N.T. Hahn, A.J. Bard, C.B. Mullins, *J Am Chem Soc*, **2012**, 134, 3659-3662.
- [79] I. Nam, N.D. Kim, G.P. Kim, J. Park, J. Yi, *J Power Sources*, **2013**, 244, 56-62.
- [80] V. Etacheri, R. Marom, R. Elazari, G. Salitra, D. Aurbach, *Energ Environ Sci*, **2011**, 4, 3243-3262.
- [81] Y.Q. Wang, Z.Z. Yang, Y.M. Qian, L. Gu, H.S. Zhou, *Adv Mater*, **2015**, 27, 3915.
- [82] L.L. Peng, Y. Zhu, D.H. Chen, R.S. Ruoff, G.H. Yu, *Adv Energy Mater*, **2016**, 6.
- [83] B. Dunn, H. Kamath, J.M. Tarascon, *Science*, **2011**, 334, 928-935.
- [84] D. Larcher, J.M. Tarascon, *Nat Chem*, **2015**, 7, 19-29.
- [85] J.W. Choi, D. Aurbach, *Nat Rev Mater*, **2016**, 1.
- [86] J. Bao, W. Xu, P. Bhattacharya, M. Stewart, J.G. Zhang, W.X. Pan, *J Phys Chem C*, **2015**, 119, 14851-14860.
- [87] B.D. McCloskey, A. Valery, A.C. Luntz, S.R. Gowda, G.M. Wallraff, J.M. Garcia, T. Mori, L.E. Krupp, *J Phys Chem Lett*, **2013**, 4, 2989-2993.
- [88] R.A. Wong, A. Dutta, C.Z. Yang, K. Yamanaka, T. Ohta, A. Nakao, K. Waki, H.R. Byon, *Chem Mater*, **2016**, 28, 8006-8015.
- [89] Z.L. Wang, D. Xu, J.J. Xu, X.B. Zhang, *Chem Soc Rev*, **2014**, 43, 7746-7786.
- [90] N.N. Feng, P. He, H.S. Zhou, *Adv Energy Mater*, **2016**, 6.
- [91] K.N. Jung, J. Kim, Y. Yamauchi, M.S. Park, J.W. Lee, J.H. Kim, *J Mater Chem A*, **2016**, 4, 14050-14068.
- [92] B.Y. Xia, Y. Yan, N. Li, H.B. Wu, X.W. Lou, X. Wang, *Nat Energy*, **2016**, 1.

- [93] J. Yin, B. Fang, J. Luo, B. Wanjala, D. Mott, R. Loukrakpam, M.S. Ng, Z. Li, J. Hong, M.S. Whittingham, C.J. Zhong, *Nanotechnology*, **2012**, 23.
- [94] J.Y. Cao, S.Y. Liu, J. Xie, S.C. Zhang, G.S. Cao, X.B. Zhao, *Acs Catal*, **2015**, 5, 241-245.
- [95] F. Wu, Y. Xing, X.Q. Zeng, Y.F. Yuan, X.Y. Zhang, R. Shahbazian-Yassar, J.G. Wen, D.J. Miller, L. Li, R.J. Chen, J. Lu, K. Amine, *Adv Funct Mater*, **2016**, 26, 7626-7633.
- [96] F.J. Li, T. Zhang, H.S. Zhou, *Energ Environ Sci*, **2013**, 6, 1125-1141.
- [97] D. Aurbach, B.D. McCloskey, L.F. Nazar, P.G. Bruce, *Nat Energy*, **2016**, 1.
- [98] F.J. Li, J. Chen, *Adv Energy Mater*, **2017**, 7.
- [99] E. Carter, A.F. Carley, D.M. Murphy, *J Phys Chem C*, **2007**, 111, 10630-10638.
- [100] K. Sobanska, A. Krasowska, T. Mazur, K. Podolska-Serafin, P. Pietrzyk, Z. Sojka, *Top Catal*, **2015**, 58, 796-810.
- [101] O.A. Syzgantseva, M. Calatayud, C. Minot, *J Phys Chem C*, **2012**, 116, 6636-6644.
- [102] A.R. Puigdollers, F. Illas, G. Pacchioni, *J Phys Chem C*, **2016**, 120, 4392-4402.
- [103] E. Duverger, T. Gharbi, E. Delabrousse, F. Picaud, *Phys Chem Chem Phys*, **2014**, 16, 18425-18432.
- [104] J. Harl, L. Schimka, G. Kresse, *Phys Rev B*, **2010**, 81.
- [105] A.V. Singh, M. Ferri, M. Tamplenizza, F. Borghi, G. Divitini, C. Ducati, C. Lenardi, C. Piazzoni, M. Merlini, A. Podesta, P. Milani, *Nanotechnology*, **2012**, 23.
- [106] Y. Lu, Z.Y. Wang, S. Yuan, L.Y. Shi, Y. Zhao, W. Deng, *Rsc Adv*, **2013**, 3, 11707-11714.

- [107] A. Sinhamahapatra, J.P. Jeon, J. Kang, B. Han, J.S. Yu, *Sci Rep-Uk*, **2016**, 6.
- [108] B.D. McCloskey, A. Speidel, R. Scheffler, D.C. Miller, V. Viswanathan, J.S. Hummelshoj, J.K. Norskov, A.C. Luntz, *J Phys Chem Lett*, **2012**, 3, 997-1001.
- [109] S.J. Kang, T. Mori, S. Narizuka, W. Wilcke, H.C. Kim, *Nat Commun*, **2014**, 5.
- [110] D.W. Kim, S.M. Ahn, J. Kang, J. Suk, H.K. Kim, Y. Kang, *J Mater Chem A*, **2016**, 4, 6332-6341.
- [111] A. Christensen, E.A. Carter, *Phys Rev B*, **1998**, 58, 8050-8064.
- [112] N.E. Singh-Miller, N. Marzari, *Phys Rev B*, **2009**, 80.
- [113] L. Johnson, C.M. Li, Z. Liu, Y.H. Chen, S.A. Freunberger, P.C. Ashok, B.B. Praveen, K. Dholakia, J.M. Tarascon, P.G. Bruce, *Nat Chem*, **2014**, 6, 1091-1099.
- [114] A. Khetan, A. Luntz, V. Viswanathan, *J Phys Chem Lett*, **2015**, 6, 1254-1259.
- [115] N. Ding, S.W. Chien, T.S.A. Hor, R. Lum, Y. Zong, Z.L. Liu, *J Mater Chem A*, **2014**, 2, 12433-12441.
- [116] R.E. Williford, J.G. Zhang, *J Power Sources*, **2009**, 194, 1164-1170.
- [117] S.N. Li, J.B. Liu, B.X. Liu, *Chem Mater*, **2017**, 29, 2202-2210.
- [118] D.Y. Zhai, H.H. Wang, J.B. Yang, K.C. Lau, K.X. Li, K. Amine, L.A. Curtiss, *J Am Chem Soc*, **2013**, 135, 15364-15372.
- [119] N. Bayal, B. Singh, R. Singh, V. Polshettiwar, *Sci Rep-Uk*, **2016**, 6.
- [120] G.P. Kim, S. Bae, M. Lee, H.D. Song, J. Yi, *Nano Energy*, **2015**, 12, 675-685.

국 문 초 록

녹색 에너지에 대한 수요와 관심의 증가에 따라 전지자동차와 에너지 그리드용 에너지 저장장치의 시장이 매우 커질 것으로 예상되며, 이는 곧 중·대형 배터리 시장의 확대로 이어질 것이다. 리튬이온배터리는 에너지와 출력 밀도가 높아 대용량 에너지를 저장하는 데에 가장 적합한 시스템이다. 그러나 중·대형 배터리로 사용되기 위해서는 안전 문제를 해결할 필요가 있으며, 더 높은 에너지 밀도를 확보하기 위한 방안이 필요하다. 본 논문에서는 안전한 리튬이온배터리를 위해 고성능의 리튬 티타네이트 (LTO) 양극재를 제안하고, 고에너지 밀도의 차세대 배터리 시스템으로 리튬산소전지를 연구하였다.

높은 안전성을 보이는 LTO의 단점인 낮은 전도성을 향상시키기 위하여 LTO-나노그래핀 혼성화 구조를 제안하였다. 양친매성 용매를 사용하여 친수성 LTO와 소수성 나노그래핀 사이에 가교를 이어줄 수 있었고, 산화환원쌍을 통하여 그래핀으로 뒤덮인 LTO를 합성하였다. 그 결과 만들어진 물질은 그래핀의 전도성으로 인하여 높은 출력 특성을 보였다.

리튬산소전지는 에너지 밀도가 높아, 한계에 다다른 리튬이온전지의 성능을 뛰어넘을 수 있을 것으로 예상된다. 그러나 충방전 반응의

가역성이 낮아 수명이 짧다는 문제점이 존재한다. 따라서 반응의 가역성을 개선하고 부반응을 억제하기 위하여 리튬산소전지의 반응기작에 대한 열역학적 접근법과 속도론적 접근법을 연구하였다.

열역학적 접근법에서는 백금을 지르코니아에 담지한 촉매를 사용하였다. 리튬산소전지의 충방전 과정 중, 친핵성이 높아 부반응을 일으키는 초과산화물과 과산화물이 생성되는데, 지르코니아 담지체가 두 물질과 결합하여 안정화시키고, 부반응을 억제시킨다는 것을 확인하였다.

운동학적 접근법에서는 방전 생성물의 조성을 변화시키는 방법을 연구하였다. 촉매의 구조적인 제어를 통하여 전해질의 확산을 억제하고 반응물 간의 접촉을 막아, 높은 과전압을 보이는 방전 생성물이 형성되는 속도를 감소시켰다. 그 결과 낮은 전압에서 충전이 진행되어 리튬산소전지의 수명이 증가하였다.

주요어: 차세대전지, 리튬이온전지, 리튬 티타네이트, 그래핀, 리튬산소전지, 반응기작, 양극 촉매

학 번: 2013-22524

List of publications

International Publications

International Academic Published Papers (First Author)

1. **S. Bae**, Y. G. Yoo, J. Park, S. Park, I. Nam, J. W. Han, and J. Yi, Platinum catalyst deposited on zirconia support for the design of lithium-oxygen battery with enhanced cycling ability, *Chemical Communications*, **2017**, 53, 11767-11770.
2. **S. Bae**, I. Nam, S. Park, Y. G. Yoo, J. Park, J. M. Lee, J. W. Han, and J. Yi, Sponge-like $\text{Li}_4\text{Ti}_5\text{O}_{12}$ constructed on graphene for high Li electroactivities, *Journal of Nanoscience and Nanotechnology*, **2017**, 17, 588-593.
3. **S. Bae***, Y. G. Yoo*, I. Nam, S. park, J. Park, J. M. Lee, J. W. Han, and J. Yi (*co-first author), Tunable Lithium Storage Properites of Metal Lithium Titanates by Stoichiometric Modulation , *Electrochemistry Communications*, **2016**, 64, 26-29.

4. **S. Bae***, I. Nam*, S. Park, Y. G. Yoo, S. Yu, J. M. Lee, J. W. Han, and J. Yi (*co-first author), Interfacial Adsorption and Redox Coupling of $\text{Li}_4\text{Ti}_5\text{O}_{12}$ with Nano-graphene for High-Rate Lithium Storage, *ACS Applied Materials & Interfaces*, **2015**, 7, 16565-16572.
5. I. Nam*, **S. Bae***, S. Park, Y. G. Yoo, J. M. Lee, J. W. Han and J. Yi (*co-first author), Omnidirectionally stretchable, high performance supercapacitors based on a graphene-carbon-nanotube layered structure, *Nano Energy*, **2015**, 15, 33-42.
6. **S. Bae**, H. D. Song, I. Nam, G. -P. Kim, J. M. Lee, and J. Yi, Quantitative Performance Analysis of Graphite- LiFePO_4 Battery Working at Low Temperature, *Chemical Engineering Science*, **2014**, 118, 74-82.

International Academic Published Papers (Co-author)

1. Y. G. Yoo*, J. Park*, H. N. Umh, S. Y. Lee, **S. Bae**, Y. H. Kim, S. E. Jerng, Y. Kim, J. Yi (*co-first author), Evaluating the environmental

- impact of the lead species in perovskite solar cells via environmental-fate modeling, *Journal of Industrial and Engineering Chemistry*, **2019**, 70, 453-461.
2. Y. G. Yoo*, S. Park*, **S. Bae**, J. Park, I. Nam, and J. Yi (*co-first author), Transition Metal-Free Graphene Framework Based on Disulfide Bridges as a Li Host Material, *Energy Storage Materials*, **2017**, 14, 238-245.
 3. I. Nam*, J. Park*, S. Park, **S. Bae**, Y. G. Yoo, J. W. Han, and J. Yi (*co-first author), Observation of crystalline change of titanium dioxide during lithium insertion by visible spectrum analysis, *Physical Chemistry Chemical Physics*, **2017**, 19, 13140-13146
 4. I. Nam, J. Park, **S. Bae**, S. Park, Y. G. Yoo, and J. Yi, Energy Storage Systems Based on Endoskeleton Structuring, *Journal of Materials Chemistry A*, **2016**, 4, 13228-13234.
 5. S. Park*, Y. G. Yoo*, I. Nam, **S. Bae**, J. Park, J. W. Han, and J. Yi (*co-first author), Insights into the Li Diffusion Dynamics and Nanostructuring of $\text{H}_2\text{Ti}_{12}\text{O}_{25}$ to Enhance Its Li Storage Performance.

ACS Applied Materials & Interfaces, **2016**, 8(19), 12186-12193.

6. G.-P. Kim*, M. Lee*, H. D. Song, **S. Bae**, and J. Yi (*co-first author), Highly efficient supporting material derived from used cigarette filter for oxygen reduction reaction , *Catalysis Communications*, **2016**, 78, 1-6.
7. G.-P. Kim, M. Lee, Y. J. Lee, **S. Bae**, H. D. Song, I. K. Song, and J. Yi, Polymer-mediated synthesis of a nitrogen-doped carbon aerogel with highly dispersed Pt nanoparticles for enhanced electrocatalytic activity, *Electrochimica Acta*, **2016**, 193, 137-144.
8. I. Nam*, J. Park*, S. Park, **S. Bae**, Y. G. Yoo, and J. Yi (*co-first author), Dual Planar-Helix Type Energy Storage Wires to Circumvent Universal Energy Lag Effect, *Advanced Energy Materials*, **2016**, 6, 1501812.
9. G.-P. Kim, **S. Bae**, M. Lee, H. D. Song, and J. Yi, Decoration of a bio-inspired carbon nanosphere with Pt nanoparticles via a polymer-assisted strategy for enhanced electrocatalytic activity, *Nano Energy*, **2015**, 12, 675-685.

10. S. Park*, Y. G. Yoo*, I. Nam, **S. Bae**, and J. Yi (*co-first author) All-Solid-State, Washable, Wearable Supercapacitors Fabricated by using a Fibrous Graphite Network and Self-Adhering Architecture, *Energy technology*, **2014** 2(8), 677-684.

Patents

1. 이종협, 남인호, **배성준**, 박수민, 유영근, 신축성 전자소자 및 에너지 저장을 위한 무기 액틴-미오신 결합, 특허 제 10-1667334호 (2016.10.12)
(특허 출원 10-2014-0175194, 2014.12.08)

International Conferences (First author)

1. Poster session, The Korean Society of Clean Technology 2014 Fall Meeting, Gyeongju, Korea, 24-26 September, 2014, **S. Bae**, I. Nam, S. Park, Y. G. Yoo, and J. Yi, Graphene wrapped $\text{Li}_4\text{Ti}_5\text{O}_{12}$ derived by the hydrophilic-hydrophobic interaction.

2. Poster session, 227th ECS Meeting, Chicago, IL, USA, 24-28, May, 2015, S. Bae, H. D. Song, I. Nam, G.-P. Kim, S. Park, Y. G. Yoo, and J. Yi, Computational analysis of battery performance working at low temperature.

International Conferences (Co-author)

1. Poster session, The 14th Japan-Korea Symposium on Catalysis, WINC Aichi, Nagoya, Japan, 1-3, July, 2013, G. -P. Kim, S. Bae, W. G. Moon, J. Park, I. Nam, S. Park, and J. Yi, Synthesis of chemically modified carbon support for platinum electrocatalysts.
2. Poster session, 2013 MRS Fall Meeting Program & Exhibit, Boston, Massachusetts, USA, 1-6, December, 2013, I. Nam, S. Park, G. -P. Kim, H. D. Song, W. G. Moon, S. Bae, and J. Yi, Fabrication of Transparent and Flexible Supercapacitor.
3. Poster session, 247th American Chemical Society National Meeting & Exposition, Dallas, Texas, USA, 16-20, March, 2014, S. Park, I. Nam, G. -P. Kim, M. Lee, W. G. Moon, S. Bae, and J. Yi, Robust hybrid film containing pseudocapacitive MnO₂ for large areal capacitance.

4. Poster session, 248th American Chemical Society National Meeting & Exposition, San Francisco, CA, USA , 10-14, August, 2014, J. Baek, T. Y. Kim, I. Nam, S. Park, S. Yu, **S. Bae**, S. Y. Lee, H. N. Umh, Y. H. Kim, and J. Yi, Production of valuable chemicals (1,3-butadiene) from biomass-based resources alternative to the petroleum.
5. Poster session, 248th American Chemical Society National Meeting & Exposition, San Francisco, CA, USA, 10-14, August, 2014, I. Nam, G.-P. Kim, S. Park, J. W. Han, **S. Bae**, S. Yu, H. N. Umh, S. Y. Lee, Y. H. Kim, and J. Yi, High voltage energy storage systems using facile patterning approach.
6. Poster session, The Korean Society of Clean Technology 2014 Fall Meeting, Gyeongju, Korea, 24-26 September, 2014, I. Nam, S. Park, G.-P. Kim, **S. Bae**, Y. G. Yoo, and J. Yi, Transparent supercapacitor solving performance reduction without percolation effect.
7. Poster session, 227th ECS Meeting, Chicago, IL, USA, 24-28, May, 2015, Y. G. Yoo, S. Park, I. Nam, **S. Bae**, and J. Yi, Wearable and washable supercapacitor based on adhering architecture.

8. Poster session, 227th ECS Meeting, Chicago, IL, USA, 24-28, May, 2015, I. Nam, G.-P. Kim, S. Park, **S. Bae**, Y. G. Yoo, J. W. Han, and J. Yi, Origami-type supercapacitor chips with high voltage performance.
9. Poster session, 19th Topical Meeting of the International Society of Electrochemistry, Auckland, New Zealand, 17-20, April. 2016, J. Yi, **S. Bae**, J. W. Han, J. M. Lee, I. Nam, S. Park, Y. G. Yoo, and S. Yu, Preparation and Characterization of $\text{Li}_4\text{Ti}_5\text{O}_{12}$ -graphene core-shell structure by adjusting the interfacial adsorption for the use of high-rate lithium storage
10. Poster session, The 15th Korea-Japan Symposium on Catalysis, BEXCO Busan, Korea, 26-28, May, 2016, M. Lee, G.-P. Kim, H. D. Song, **S. Bae**, and J. Yi, Used-Cigarette Filter Induced Electrocatalytic Carbon Support for Efficient Reduction of Oxygen.
11. Poster session, 2016 MRS Fall Meeting Program & Exhibit, Boston, MA, USA, Nov. 27-Dec. 2, 2016, Y. G. Yoo, S. Park, **S. Bae**, I. Nam, J. Park, J. W. Han, and J. Yi, Nanostructuring of $\text{H}_2\text{Ti}_{12}\text{O}_{25}$ for High-Voltage Lithium-Ion Battery Anodes Based on Theoretical Studies.

12. Poster session, 2016 MRS Fall Meeting Program & Exhibit, Boston, MA, USA, Nov. 27-Dec. 2, 2016, J. Park, I. Nam, S. Park, **S. Bae**, Y. G. Yoo, and J, Yi, Plane Integrated Supercapacitor Wires without Energy Limitations.

Domestic Conferences

1. 2013년 한국청정기술학회 춘계 학술발표회, 여수, 28-29, 3, 2013, 박수민, 김길표, 남인호, 박준수, **배성준**, 문원균, 이종협, 금속 산화물/유기젤 하이브리드 전극 제조와 박막형 슈퍼커패시터에의 응용.
2. 한국전기화학회 2013년도 춘계총회 및 학술발표회, 창원, 11-13, 4, 2013, 박수민, 남인호, 김길표, 박준수, **배성준**, 이종협, 고효율 슈퍼커패시터 전극을 위한 삼차원 구조의 금속/탄소 복합체 제조.
3. 2013년 한국청정기술학회 추계 학술발표회, 제주, 25-27, 9, 2013, 남인호, 박수민, 김길표, 문원균, **배성준**, 송현돈, 이종협, 아가로스 겔을 이용한 삼차원 금속/탄소 복합체 제조 및 고효율 슈퍼커패시터로의 응용.
4. 한국전기화학회 2013년 추계 총회 및 학술발표회, 대전, 7-9, 11, 2013, 남인호, 김길표, 박수민, 송현돈, 이민재, 문원균, **배성준**, 이종협, 대면적의 패터화된 망간 산화물 슈퍼커패시터 개발 및 성능 평가.

5. 한국전기화학회 2013년 추계 총회 및 학술발표회, 대전, 7-9, 11, 2013, 박수민, 남인호, 김길표, 문원균, **배성준**, 이민재, 송현돈, 이종협, 박막전지의 구조적 안정성을 높이기 위한 유기겔-금속산화물 복합체 합성.
6. 한국전기화학회 2013년 추계 총회 및 학술발표회, 대전, 7-9, 11, 2013, 김길표, 박수민, 남인호, 송현돈, 이민재, **배성준**, 문원균, 이종협, 전기화학 증착법을 이용한 이방성 결정구조를 지닌 연결된 기공구조의 NiO 합성 및 리튬이온 배터리 음극 활용.
7. 2014년 한국청정기술학회 춘계 학술발표회, 여수, 27-28, 3, 2014, **배성준**, 송현돈, 남인호, 김길표, 이종민, 이종협, 수치해석을 통한 리튬 이온 전지 활물질 특성 평가.
8. 2014년 한국청정기술학회 춘계 학술발표회, 여수, 27-28, 3, 2014, 박수민, 유영근, 남인호, **배성준**, 이종협, 전도성 탄소 네트워크 제조 및 슈퍼커패시터 전극으로서 응용.
9. 한국전기화학회 2014년 춘계 총회 및 학술발표회, 창원, 10-12, 4, 2014, 박수민, 유영근, 남인호, **배성준**, 이종협, 접착성 기판을 이용한 전도성 탄소 네트워크의 제조 및 이를 이용한 접을 수 있는 슈퍼커패시터 개발.
10. 한국전기화학회 2014년 춘계 총회 및 학술발표회, 창원, 10-12, 4, 2014, **배성준**, 남인호, 송현돈, 김길표, 이종민, 이종협, 수치해석을 통한

저온에서 리튬 이온 전지의 성능 최적화.

11. 한국화학공학회 2014년도 가을 총회 및 학술대회, 대전, 23-24, 10, 2014,
이수영, 유성주, 엄하늬, 남인호, **배성준**, 한정우, 이종협, 인공광합성
시스템하에서의 전하 이동 및 표면 반응 메커니즘.
12. 한국화학공학회 2014년도 가을 총회 및 학술대회, 대전, 23-24, 10, 2014,
남인호, 김길표, 박수민, **배성준**, 유영근, 최경희, 이종협, 환경 분석용
휴대전자기기를 위한 투명한 에너지 저장 시스템 개발.
13. 한국화학공학회 2014년도 가을 총회 및 학술대회, 대전, 23-24, 10, 2014,
박수민, 유영근, 남인호, **배성준**, 이종협, 수계 환경 분석용 전자기기를
위한 방수성 에너지 저장 시스템 개발.
14. 한국화학공학회 2015년도 가을 총회 및 학술대회, 일산, 21-23, 10, 2015,
남인호, **배성준**, 박수민, 유영근, 박종석, 한정우, 이종협, 신축성 전자소자
및 에너지 저장을 위한 그래핀-탄소나노튜브 복합전극 개발.
15. 한국화학공학회 2015년도 가을 총회 및 학술대회, 일산, 21-23, 10, 2015,
배성준, 남인호, 박수민, 유영근, 유성주, 박종석, 한정우, 이종협, 용매와의
상호작용에 따른 그래핀-LTO 복합체의 형태변화 및 전기화학적 성능
분석.
16. 한국전기화학회 2016년 춘계 총회 및 학술발표회, 광주, 7-9, 4, 2016, **배성준**,

남인호, 박수민, 유영근, 박종석, 한정우, 이종협, $\text{Li}_4\text{Ti}_5\text{O}_{12}$ 의 리튬저장능력 향상을 위한 다공성 구조 및 그래핀 복합체 구현.

17. 한국전기화학회 2016년 춘계 총회 및 학술발표회, 광주, 7-9, 4, 2016, 유영근, **배성준**, 남인호, 박수민, 박종석, 한정우, 이종협, $\text{MLi}_2\text{Ti}_6\text{O}_{14}$ (M=2 Na, Sr) 리튬 배터리 음극재의 전기화학적 특성 분석 및 조절.
18. 한국전기화학회 2016년 춘계 총회 및 학술발표회, 광주, 7-9, 4, 2016, 남인호, 박종석, 박수민, **배성준**, 유영근, 이종협, 평면 나선형 구조 발현을 통한 1차원 슈퍼캐패시터의 내재적 성능 개선.
19. 한국화학공학회 2016년도 봄 총회 및 학술대회, 부산, 27-29, 4, 2016, 이민재, 김길표, 이윤재, **배성준**, 송현돈, 송인규, 윤양식, 김윤화, 이종협, 탄소 에어로겔의 고분자 기능화를 통한 고분산 백금 나노촉매 개발 및 전기화학적 성능평가.
20. 한국화학공학회 2016년도 가을 총회 및 학술대회, 대전, 19-21, 10, 2016, 박종석, **배성준**, 남인호, 박수민, 이종협, 내골격 구조를 통한 에너지 저장 장치 설계의 새로운 접근.
21. 한국화학공학회 2017년도 봄 총회 및 학술대회, 제주, 26-28, 4, 2017, **배성준**, 유영근, 박종석, 송현돈, 엄하늬, 이수영, 김용화, 정성은, 이종협, 한정우, 지르코니아 표면 특성으로 인한 리튬산소전지의 방전생성물 안정화 연구.

22. 한국화학공학회 2017년도 가을 총회 및 학술대회, 대전, 25-27, 10, 2017, 박종석, **배성준**, 유영근, 이종협, 남인호, 박수민, 한정우, 이산화티탄 내리튬 삽입 시의 구조색 변화를 통한 실시간 결정구조 분석.
23. 페로브스카이트 포토닉스 학술대회, 제주, 20-21, 11, 2017, 이수영, 엄하늬, **배성준**, 유영근, 박종석, 김용화, 정성은, 김영훈, 최진희, 이종협, Environmental Safety Assessment of Perovskite Solar Cell.
24. 페로브스카이트 포토닉스 학술대회, 제주, 20-21, 11, 2017, 김용화, 정성은, 유영근, 박종석, 엄하늬, **배성준**, 이수영, 김영훈, 최진희, 이종협, Environmental Impact Analysis of Perovskite and Silicon Solar Cell via Life-cycle Assessment.